

## Enabling ultrafast ionic conductivity in Br-based lithium argyrodite electrolytes for solid-state batteries with different anodes

Chuang Yu<sup>a</sup>, Yong Li<sup>b</sup>, Weihan Li<sup>a</sup>, Keegan R. Adair<sup>a</sup>, Feipeng Zhao<sup>a</sup>, Mathew Willans<sup>c</sup>, Jianwen Liang<sup>a</sup>, Yang Zhao<sup>a</sup>, Changhong Wang<sup>a</sup>, Sixu Deng<sup>a</sup>, Ruying Li<sup>a</sup>, Huan Huang<sup>d</sup>, Shigang Lu<sup>e</sup>, Tsun-Kong Sham<sup>c</sup>, Yining Huang<sup>c,\*,\*\*</sup>, Xueliang Sun<sup>a,\*</sup>

<sup>a</sup> Department of Mechanical and Materials Engineering, The University of Western Ontario, London, Ontario, N6A 5B9, Canada

<sup>b</sup> Institute of Applied and Physical Chemistry and Center for Environmental Research and Sustainable Technology, University of Bremen, 28359 Bremen, Germany

<sup>c</sup> Department of Chemistry, The University of Western Ontario, 1151 Richmond Street, London, Ontario, N6A 5B7, Canada

<sup>d</sup> Glabat Solid-State Battery Inc., 700 Collip Circle, London, Ontario, N6G 4X8, Canada

<sup>e</sup> China Automotive Battery Research Institute Co. Ltd, 5th Floor, No. 43, Mining Building, North Sanhuan Middle Road, Haidian District, Beijing, 100088, China

### ARTICLE INFO

#### Keywords:

Synthesis

Lithium argyrodite

Ionic conductivity

Anode compatibility

Solid-state batteries

### ABSTRACT

One of the primary obstacles that has inhibited the development of solid-state batteries is the lower conductivity of solid electrolytes compared to liquid electrolytes.  $\text{Li}_6\text{PS}_5\text{Br}$  is a promising solid electrolyte for solid-state batteries due to its high ionic conductivity and low cost. Herein, we enhance the lithium conductivity by replacing S with Br and systematically tailor the composition and synthesis parameters to optimize the conductivity.  $\text{Li}_{5.5}\text{PS}_{4.5}\text{Br}_{1.5}$  exhibits higher ionic conductivity and better lithium compatibility than the bare  $\text{Li}_6\text{PS}_5\text{Br}$ . Although lithium metal is chemically unstable with  $\text{Li}_{5.5}\text{PS}_{4.5}\text{Br}_{1.5}$ , stable cycling behavior in lithium symmetrical cells with small overpotential and resistance after 2500 h are achieved. Both the bare NCM622 and  $\text{LiNbO}_3$ -coated NCM622 shows long cycling life with  $\text{Li}_{5.5}\text{PS}_{4.5}\text{Br}_{1.5}$  electrolyte in combination with In or lithium metal anodes. The  $\text{LiNbO}_3$  layer can effectively improve the capacity and cycling behavior of the solid-state battery using different anodes. Moreover, the electrochemical performances of  $\text{Li}_{5.5}\text{PS}_{4.5}\text{Br}_{1.5}$ -based solid-state batteries are influenced by the charge/discharge voltage windows.

### 1. Introduction

Lithium-ion batteries have attracted significant attention over the past decades due to their high energy and power densities [1–4]. Currently, the application of lithium-ion battery in electric vehicles (EVs) has raised new requirements, such as even higher energy density, improved safety, and extremely long cycle life [5,6]. However, the flammable organic liquid electrolyte used in the current lithium-ion battery suffer from safety issues and traditional Li-ion batteries have nearly reached their physicochemical energy density limit [5,6]. To fulfill the above requirements, replacing the organic liquid electrolyte with the inflammable inorganic solid electrolyte is a possible way to improve safety characteristics and enhance the energy density [6,7].

Unlike liquid electrolytes, the lithium ions in the solid electrolyte deliver a lower lithium ion conductivity, which has impeded the development of solid-state batteries [6,8]. Among the inorganic solid

electrolytes, lithium argyrodite  $\text{Li}_6\text{PS}_5\text{X}$  (X = Cl, Br, and I) provides acceptable room temperature lithium ion conductivities ( $\sim 10^{-3}$  S/cm) via simple synthesis routes using low-cost raw materials, which makes it a promising solid electrolyte candidate for application in solid-state batteries [9–17]. Although the ionic conductivity of lithium argyrodite is higher than most of the inorganic electrolytes, it is still one order of magnitude lower than the conductivity of organic liquid electrolyte ( $10^{-3}$  vs.  $10^{-2}$  S/cm) [9–13]. Significant efforts have been put forward to promote enhanced ionic conductivity in lithium argyrodites [11,13, 18–20]. One typical method to enhance the ionic conductivity of lithium argyrodites is through elemental substitutions [18–22]. The substitution of P with other elements, such as Ge, Si, and Sn, can greatly enhance the ionic conductivity in lithium argyrodite due to the site disorder [20,22]. By increasing the Ge content in  $\text{Li}_{6+x}\text{P}_{1-x}\text{Ge}_x\text{S}_5\text{I}$ , the lithium ion conductivity of lithium argyrodite was increased to  $5.4 \pm 0.8$  mS/cm in a cold-pressed state and  $18.4 \pm 2.7$  mS/cm upon sintering [22]. Besides the

\* Corresponding author.,

\*\* Corresponding author.

E-mail addresses: [yhuang@uwo.ca](mailto:yhuang@uwo.ca) (Y. Huang), [xsun9@uwo.ca](mailto:xsun9@uwo.ca) (X. Sun).

<https://doi.org/10.1016/j.ensm.2020.04.014>

Received 10 February 2020; Received in revised form 24 March 2020; Accepted 13 April 2020

Available online 1 May 2020

2405-8297/© 2020 Elsevier B.V. All rights reserved.

substitutions of P sites, another effective strategy is to replace S with Se [18] or Cl [23], which can greatly promote higher ionic conductivity. The optimal composition for Cl-substituted  $\text{Li}_6\text{PS}_5\text{Cl}$ ,  $\text{Li}_{5.5}\text{PS}_{4.5}\text{Cl}_{1.5}$ , delivers an ionic conductivity of  $9.4 \pm 0.1$  mS/cm at room temperature [23]. Our previous research has also shown that  $\text{Li}_{5.7}\text{PS}_{4.7}\text{Cl}_{1.3}$  shows a room temperature conductivity of 6.4 mS/cm [24]. The ionic radius of  $\text{Br}^-$  (1.96 Å) is much larger than that of  $\text{Cl}^-$  (1.81 Å), leading to greater difficulty in substituting  $\text{S}^{2-}$  (1.84 Å) with  $\text{Br}^-$  in  $\text{Li}_6\text{PS}_5\text{Br}$ . However, the replacement of  $\text{S}^{2-}$  (1.84 Å) with  $\text{Br}^-$  (1.96 Å) is a possible route to enhance the lithium ion conductivity in  $\text{Li}_6\text{PS}_5\text{Br}$ .

Li metal has attracted the attention of many researchers due to its high theoretical capacity (3860 mA h/g) and low electrochemical potential ( $\sim -3.040$  V), providing the possibility to achieve both higher gravimetric and volumetric energy densities [25–27]. However, previous papers have shown that the Li/lithium argyrodite interface is unstable due to the weak bonding between P and S in lithium argyrodites, which can be easily decomposed when they are in contact with Li-metal [28–31]. When in contact with Li metal, lithium argyrodites will decompose into an interphase composed of  $\text{Li}_3\text{P}$ ,  $\text{Li}_2\text{S}$ , and  $\text{LiX}$  ( $X = \text{Cl}$  and  $\text{Br}$ ), which can act as an SEI layer and conduct lithium ions between lithium metal and the lithium argyrodite electrolyte layer [31]. This gives the possibility to assemble solid-state lithium metal batteries using lithium argyrodite solid electrolytes. Nevertheless, very few research works have been reported based on lithium argyrodite solid-state lithium metal batteries [32]. Whether lithium argyrodite-based solid-state Li metal batteries is feasible remains unknown.

In this work, we propose an effective route to enhance the conductivity  $\text{Li}_6\text{PS}_5\text{Br}$  by replacing S with Br. The introduction of the Br amount in  $\text{Li}_6\text{PS}_5\text{Br}$  is tailored to achieve the optimal lithium ion conductivity. We have found that  $\text{Li}_{5.5}\text{PS}_{4.5}\text{Br}_{1.5}$  shows the highest lithium ion conductivity among Br-based lithium argyrodites and its analogues.

The detailed mechanism of the improved conductivity for  $\text{Li}_{5.5}\text{PS}_{4.5}\text{Br}_{1.5}$  compared to  $\text{Li}_6\text{PS}_5\text{Br}$  is unraveled by AC impedance spectroscopy,  $^7\text{Li}$  NMR, and AIMD simulations. Synchrotron-based X-ray absorption near-edge spectroscopy and EIS as a function of storage durations are employed to investigate the lithium compatibility of  $\text{Li}_{5.5}\text{PS}_{4.5}\text{Br}_{1.5}$  under different conditions. Solid-state batteries using  $\text{Li}_{5.5}\text{PS}_{4.5}\text{Br}_{1.5}$  electrolyte in combination with the bare NCM622 and  $\text{LiNbO}_3$ -coated NCM622 with In and lithium metal anode are fabricated for the investigation of electrochemical performances under various charge/discharge voltage windows.

## 2. Experimental

**Sample preparations.** Reagent-grade  $\text{Li}_2\text{S}$  (99.98%, Sigma-Aldrich),  $\text{P}_2\text{S}_5$  (99%, Sigma-Aldrich), and  $\text{LiBr}$  (99.0%, Sigma-Aldrich) crystalline powders were used as starting materials. The weight ratio of these starting materials was weighed based on the target composition  $\text{Li}_{7-x}\text{PS}_{6-x}\text{Br}_x$  ( $x = 1.0, 1.1, 1.2, 1.3, 1.4, 1.5, 1.6, \text{ and } 1.7$ ). The required amount of the starting materials was sealed in a  $\text{ZrO}_2$  jar with 16 ( $\varphi = 10$  mm) large  $\text{ZrO}_2$  balls and 16 ( $\varphi = 5$  mm) small  $\text{ZrO}_2$  balls in an argon-filled glovebox due to the oxygen and moisture sensitivity of the mixture. The total amount of the mixture was fixed at 3.0 g. The milling speed was fixed at 500 rpm and the total milling time was 15 h. The mechanical milling process was performed according to our previous paper [12,13]. After the milling process, the obtained mixture was first pressed into a pellet and then sealed in the quartz tubes, followed by annealing at various temperatures (250, 350, 400, 500 °C, and 550 °C) for 5 h. For  $\text{Li}_{5.5}\text{PS}_{4.5}\text{Br}_{1.5}$ , the precursor annealed at 400 °C for 10 h was chosen as the solid electrolyte for solid-state batteries.

**Structure and morphology characterizations.** Powder XRD patterns were collected over a  $2\theta$  range of 10–80° to identify the crystalline phases of the different samples using  $\text{CuK}\alpha$  X-rays ( $\lambda = 1.54178$  Å) on Bruker AXS D8. To prevent reaction with moisture and oxygen, the powders were sealed by Kapton foil in an Argon filled glove box. The P and S K-edge XANES spectra were collected at the Soft X-ray Micro-Characterization

Beamline (SXRMB) at the Canadian Light Source with the fluorescence yield (FLY) mode. A Hitachi S-4800 scanning electron microscope accompanied by an energy-dispersive X-ray scattering system was chosen to probe the elemental distribution of the solid electrolyte.

**Li-ion dynamics characterizations.** The ionic conductivity of the mixture annealed at various temperatures was determined by AC impedance spectroscopy. Indium foils ( $\varphi = 10$  mm) were chosen as the blocking electrodes and attached on both faces of the 10 mm diameter powder pellet. AC impedance measurements were performed on the versatile multichannel potentiostat 3/Z (VMP3) in the frequency range of 1 Hz–7 MHz with an applied voltage of 0.02 V.

Solid-state NMR measurements were performed using a Varian Infinity Plus 400 NMR spectrometer equipped with an Oxford AS400 wide-bore magnet ( $B_0 = 9.4$  T) and a Varian stationary-sample HX 5.0 mm probe. The  $^7\text{Li}$  Larmor frequency was 155.248 MHz. The  $\pi/2$  and  $\pi$  pulse lengths were determined to be 2.1 and 4.4  $\mu\text{s}$ , respectively. Chemical shifts were referenced with respect to a 1.0 M LiCl solution. The samples were sealed in custom-made Teflon tubes ( $\varphi = 4.7$  mm) in an argon-filled glovebox ( $\text{H}_2\text{O}, \text{O}_2 < 0.1$  ppm). The  $^7\text{Li}$  spin-lattice relaxation times ( $T_1$ ) were determined using an inversion-recovery NMR method where the experimental data was fit to a 3-parameter inversion-recovery equation using the Chemagnetics Spinsight NMR software package. For the  $T_1$  determinations, between 10 and 2000 tau values were utilized and the recycle delays were set to a minimum of 5 times the determined  $T_1$  values. The AIMD simulations were performed according to our previous work [24].

**Electrochemical Measurements.** The electrochemical performance of  $\text{Li}_{5.5}\text{PS}_{4.5}\text{Br}_{1.5}$  was investigated by fabricating laboratory-scale solid-state batteries with model pressure cells. Commercial  $\text{LiNi}_{0.6}\text{Mn}_{0.2}\text{Co}_{0.2}\text{O}_2$  (Named NCM622 for short) was purchased from China Automotive Battery Research Institute, China and the  $\text{LiNbO}_3$ -coated  $\text{LiNi}_{0.6}\text{Mn}_{0.2}\text{Co}_{0.2}\text{O}_2$  was prepared using ALD as our previous work [33]. The cathode mixture was prepared by hand mixing the bare NCM622 or  $\text{LiNbO}_3$ -coated NCM622 with  $\text{Li}_{5.5}\text{PS}_{4.5}\text{Br}_{1.5}$  with a weight ratio of 7/3. Indium foil and lithium metal were chosen as the anode materials for  $\text{Li}_{5.5}\text{PS}_{4.5}\text{Br}_{1.5}$ -based solid-state batteries, respectively. 10–11 mg of the cathode mixture was pressed together with 100 mg of  $\text{Li}_{5.5}\text{PS}_{4.5}\text{Br}_{1.5}$  to make a bilayer pellet ( $\varphi = 10$  mm) under a pressure of 5 tons. A piece of In foil or Li metal foil was attached on the other side of the bilayer to form a triple-layer pellet. The solid-state batteries using In foil and Li metal foil was cycled at 0.255 mA/cm<sup>2</sup> ( $\sim 0.2\text{C}$ ) and 0.127 mA/cm<sup>2</sup> ( $\sim 0.1\text{C}$ ) respectively on LAND battery testing station under various charge/discharge voltage windows. The galvanostatic intermittent titration technique (GITT) measurements were conducted with a current density of 0.127 mA/cm<sup>2</sup> on LAND battery testing station and the cyclic voltammetry (CV) measurements of solid-state batteries using In and Li metal were performed at different voltage windows with a scan rate of 0.08 mV/s on the versatile multichannel potentiostat 3/Z (VMP3). All of these electrochemical measurements were conducted at room temperature. The capacity in this work was calculated based on the weight of the active material in the cathode mixture.

## 3. Results and discussion

$\text{Li}_6\text{PS}_5\text{X}$  ( $X = \text{Cl}, \text{Br}$ ) has been synthesized directly by mechanical milling with a Fritsch 7 mill [12,13]. However, the structure of processor in this work after high rotation ball milling (550 rpm/16 h) is not the cubic F-43 m phase even after choosing the same total number of balls and starting materials weight ratio, suggesting that to obtain the pure lithium argyrodite by directly milling process is highly dependent on the milling apparatus and the materials of balls and jars. To obtain pure  $\text{Li}_6\text{PS}_5\text{Br}$  with the highest ionic conductivity, the milled mixture was annealed at various temperatures (250, 350, 400, 500 °C, and 550 °C) for 5 h. As shown in Fig. 1a, the room temperature lithium ion conductivities of  $\text{Li}_6\text{PS}_5\text{Br}$  annealed at various temperatures are  $5.28 \times 10^{-4}$  S/cm for 250 °C,  $7.37 \times 10^{-4}$  S/cm for 350 °C,  $6.86 \times 10^{-4}$  S/cm for 400 °C,  $6.61$

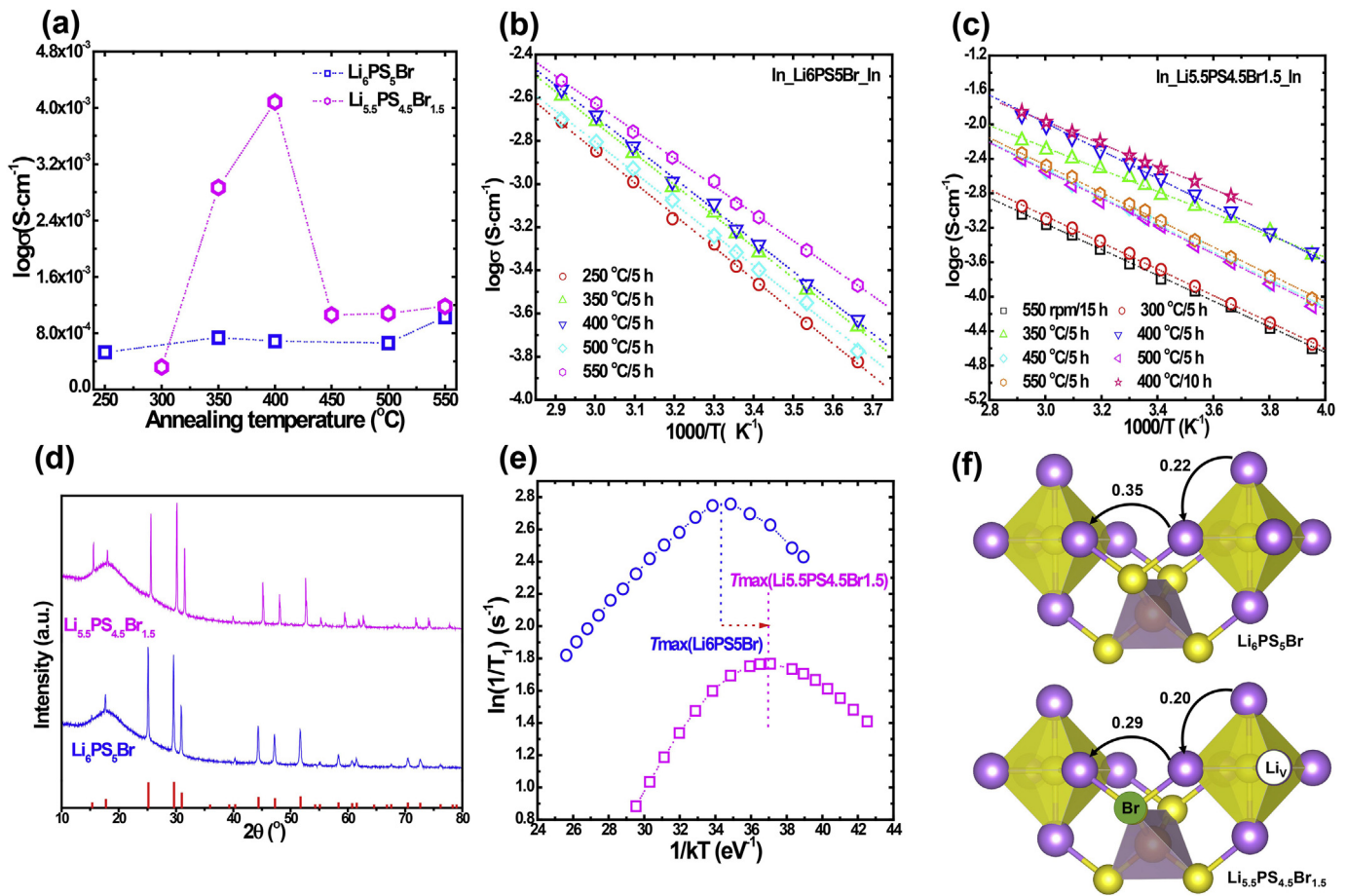


**Fig. 1.** (a) The room-temperature ionic conductivities of  $\text{Li}_6\text{PS}_5\text{Br}$  and  $\text{Li}_{5.5}\text{PS}_{4.5}\text{Br}_{1.5}$  annealed at various temperatures for 5 h. (b) The Arrhenius plots of  $\text{Li}_6\text{PS}_5\text{Br}$  annealed at various temperatures for 5 h. (c) The Arrhenius plots of the mechanical milled (550 rpm/16 h) and annealed  $\text{Li}_{5.5}\text{PS}_{4.5}\text{Br}_{1.5}$  at various temperatures for 5 h. The plot of  $\text{Li}_{5.5}\text{PS}_{4.5}\text{Br}_{1.5}$  annealed at 400 °C for 10 h is also shown for comparison. (d) XRD diffraction patterns of  $\text{Li}_6\text{PS}_5\text{Br}$  annealed at 550 °C for 5 h and  $\text{Li}_{5.5}\text{PS}_{4.5}\text{Br}_{1.5}$  annealed at 400 °C for 10 h. (e) Temperature-dependent  $^7\text{Li}$  spin-lattice relaxation time ( $T_1$ ) changes of the corresponding  $\text{Li}_6\text{PS}_5\text{Br}$  and  $\text{Li}_{5.5}\text{PS}_{4.5}\text{Br}_{1.5}$ . (f) Simulation results of  $\text{Li}_6\text{PS}_5\text{Br}$  and  $\text{Li}_{5.5}\text{PS}_{4.5}\text{Br}_{1.5}$ . Indium foil was chosen as the blocking electrode in the measurements.

$\times 10^{-4}$  S/cm for 500 °C, and  $1.03 \times 10^{-3}$  S/cm for 550 °C, respectively. We previously reported that  $\text{Li}_6\text{PS}_5\text{Br}$  obtained by annealing of the pure  $\text{Li}_6\text{PS}_5\text{Br}$  at 300 °C for 5 h exhibits a lithium ion conductivity of  $1.1 \times 10^{-3}$  S/cm at room temperature [12]. Similar conductivity achieved in this work (1.03 mS/cm vs. 1.11 mS/cm) suggests that optimization of the annealing temperature can help to achieve the pure  $\text{Li}_6\text{PS}_5\text{Br}$  phase with high lithium ion conductivity, although the pure lithium argyrodite phase is not formed in the first mechanical milling process. The comparable lithium conductivity of  $\text{Li}_6\text{PS}_5\text{Br}$  obtained by annealing the precursors from the same milling route with different apparatus suggests that the milling process has a slight effect on the ionic conductivity of the final samples, while the annealing temperature has significant influence on the conductivity of lithium argyrodites, which is in good agreement with the conclusion reported by Rao et al. [16] As shown in Fig. 1b,  $\text{Li}_6\text{PS}_5\text{Br}$  annealed at 550 °C for 5 h shows much higher lithium ion conductivity at all temperatures. The corresponding activation energy of  $\text{Li}_6\text{PS}_5\text{Br}$  obtained by annealing the precursor at 550 °C deduced from temperature-dependent lithium ion conductivity is 0.296 eV. The much higher ionic conductivity of  $\text{Li}_6\text{PS}_5\text{X}$  (X = Cl and Br) compared to  $\text{Li}_7\text{PS}_6$  ( $10^{-3}$  S/cm vs.  $10^{-6}$  S/cm) is due to the replacement of  $\text{S}^{2-}$  with  $\text{Cl}^-$ , resulting in more lithium vacancies and thus yielding a higher lithium ion conductivity [9,34]. To create even more lithium vacancy in  $\text{Li}_6\text{PS}_5\text{Br}$ , part of the  $\text{S}^{2-}$  in the structure was replaced by  $\text{Br}^-$ , yielding a composition of  $\text{Li}_{5.5}\text{PS}_{4.5}\text{Br}_{1.5}$ . The precursor obtained via the mechanical milling process based on the target composition  $\text{Li}_{5.5}\text{PS}_{4.5}\text{Br}_{1.5}$  was annealed at different temperatures (300, 350, 400, 450, 500 °C, and 550

°C) for 5 h. The corresponding room temperature lithium ion conductivities of  $\text{Li}_{5.5}\text{PS}_{4.5}\text{Br}_{1.5}$  annealed at various temperatures are  $3.18 \times 10^{-4}$  S/cm for 300 °C,  $2.87 \times 10^{-3}$  S/cm for 350 °C,  $4.17 \times 10^{-3}$  S/cm for 400 °C,  $1.06 \times 10^{-3}$  S/cm for 450 °C,  $1.08 \times 10^{-3}$  S/cm for 500 °C, and  $1.18 \times 10^{-3}$  S/cm for 550 °C, respectively. The optimal annealing temperature for  $\text{Li}_{5.5}\text{PS}_{4.5}\text{Br}_{1.5}$  to achieve the highest ionic conductivity,  $4.17 \times 10^{-3}$  S/cm, is 400 °C. Meanwhile, for  $\text{Li}_6\text{PS}_5\text{Br}$ , to get the highest lithium ion conductivity ( $1.03 \times 10^{-3}$  S/cm), the optimal annealing temperature is 550 °C. Replacing  $\text{S}^{2-}$  with  $\text{Br}^-$  in  $\text{Li}_6\text{PS}_5\text{Br}$  using the classic mechanical milling followed by annealing synthesis route not only enhances the lithium ion conductivity (4.17 mS/cm vs. 1.03 mS/cm) at room temperature but also decreases the annealing temperature (400 °C vs. 550 °C). To double-check the ionic conductivity of  $\text{Li}_{5.5}\text{PS}_{4.5}\text{Br}_{1.5}$  obtained after annealing at different temperatures, the temperature-dependent lithium ion conductivity was measured and the results are shown in Fig. 1c.  $\text{Li}_{5.5}\text{PS}_{4.5}\text{Br}_{1.5}$  annealed at 400 °C for 5 h displayed much higher lithium ion conductivities among all of these annealed samples, suggesting that 400 °C is the optimal annealing temperature to achieve the highest ionic conductivity when fixing the annealing duration at 5 h. To investigate the heat treatment duration, a longer annealing time 10 h was chosen and a slightly higher lithium ion conductivity of  $4.35 \times 10^{-3}$  S/cm was achieved for  $\text{Li}_{5.5}\text{PS}_{4.5}\text{Br}_{1.5}$ . Hereby, the annealing parameters in this work for  $\text{Li}_{6-x}\text{PS}_{5-x}\text{Br}_x$  (x = 1.0, 1.1, 1.2, 1.3, 1.4, 1.5, 1.6, and 1.7) was fixed at 400 °C for 10 h. Previous simulation results have shown that the ionic conductivity of lithium argyrodite is influenced by the disorder of X (X = Cl, Br) [34], which is

also can be tailored by heat treatment [24,35], therefore optimizing the annealing parameters to produce optimal disorder in the structure is vital to obtain high conductivity. The optimal Br ordering over  $4a$  and  $4c$  sites in  $\text{Li}_6\text{PS}_5\text{Br}$  has successfully controlled by altering the annealing temperature [35], which may explain the reason  $\text{Li}_6\text{PS}_5\text{Br}$  and  $\text{Li}_{5.5}\text{PS}_{4.5}\text{Br}_{1.5}$  annealed at 550 and 400 °C show the highest ionic conductivity.  $\text{Li}_{5.5}\text{PS}_{4.5}\text{Br}_{1.5}$  annealed at 400 °C for 10 h with a lithium ion conductivity of  $4.35 \times 10^{-3}$  S/cm was chosen as the solid electrolyte for both the characterization and solid-state batteries.  $\text{Li}_{5.5}\text{PS}_{4.5}\text{Br}_{1.5}$  displays much higher lithium ion conductivity than that of  $\text{Li}_6\text{PS}_5\text{Br}$ , as shown in Fig. 1d. The activation energies derived from temperature-dependent lithium ion conductivity of  $\text{Li}_{5.5}\text{PS}_{4.5}\text{Br}_{1.5}$  and  $\text{Li}_6\text{PS}_5\text{Br}$  are quite similar to each other, 0.255 eV vs. 0.251 eV, suggesting that the energy barrier for lithium diffusion in both compositions at a long diffusion scale are almost unchanged. Considering that the above results have shown that  $\text{Li}_{5.5}\text{PS}_{4.5}\text{Br}_{1.5}$  delivers much higher lithium ion conductivity, one reason for this enhancement is due to the creation of more charge carriers after the replacement of  $\text{Br}^-$  to  $\text{S}^{2-}$ . However, it is not easy to reveal the underlying diffusion mechanism in the bulk of the lithium conductor due to the influence of porosity, grain boundaries, and effects introduced by the blocking electrode [11], while NMR is a unique characterization method to unravel lithium ion diffusion at short-range vibration time scales [10].

To investigate the intrinsic lithium ion mobility,  $^7\text{Li}$  spin-lattice relaxation (SLR) time measurements as a function of temperature were performed and the data are shown in Fig. 1e. When  $1/T_1$  reaches a maximum, the hopping frequency of lithium ion  $\tau^{-1}$  is in the order of the Larmor frequency ( $\omega_0$ ), which is decided by the atom species and the applied magnetic field strength  $B_0$  [10–12]. With a Larmor frequency of  $\omega_0/2\pi = 155.248$  MHz, the maximum relaxation rate of  $\text{Li}_{5.5}\text{PS}_{4.5}\text{Br}_{1.5}$  is reached at 313 K and the corresponding lithium ion jump frequency  $\tau_c^{-1}$  at this temperature can be deduced to be approximately  $9.75 \times 10^8$  s $^{-1}$ . Our previous work has reported that the maximum relaxation rate is reached at 358 K for  $\text{Li}_6\text{PS}_5\text{Br}$  at the Larmor frequency of 155.506 MHz. A similar lithium jump rate is achieved at a lower temperature (313 K) for  $\text{Li}_{5.5}\text{PS}_{4.5}\text{Br}_{1.5}$  compared to that of  $\text{Li}_6\text{PS}_5\text{Br}$  (358 K), suggesting that  $\text{Li}_{5.5}\text{PS}_{4.5}\text{Br}_{1.5}$  has a faster lithium ion mobility than  $\text{Li}_6\text{PS}_5\text{Br}$ . This result is in good agreement with previous impedance data. The activation energies deduced from the high-temperature and low-temperature flanks are 0.16 (7) eV and 0.08 (9) eV with an asymmetry of  $\beta = 1.533$ . AIMD simulations were performed to investigate the energy barriers for lithium diffusion in  $\text{Li}_6\text{PS}_5\text{Br}$  and  $\text{Li}_{5.5}\text{PS}_{4.5}\text{Br}_{1.5}$ , the energy barriers for lithium moves to its neighbor sites are 0.35 and 0.22 eV, while the corresponding values for  $\text{Li}_{5.5}\text{PS}_{4.5}\text{Br}_{1.5}$  are 0.29 and 0.20 eV, respectively. The replacement of  $\text{S}^{2-}$  with  $\text{Br}^-$  can greatly decrease the energy barriers for

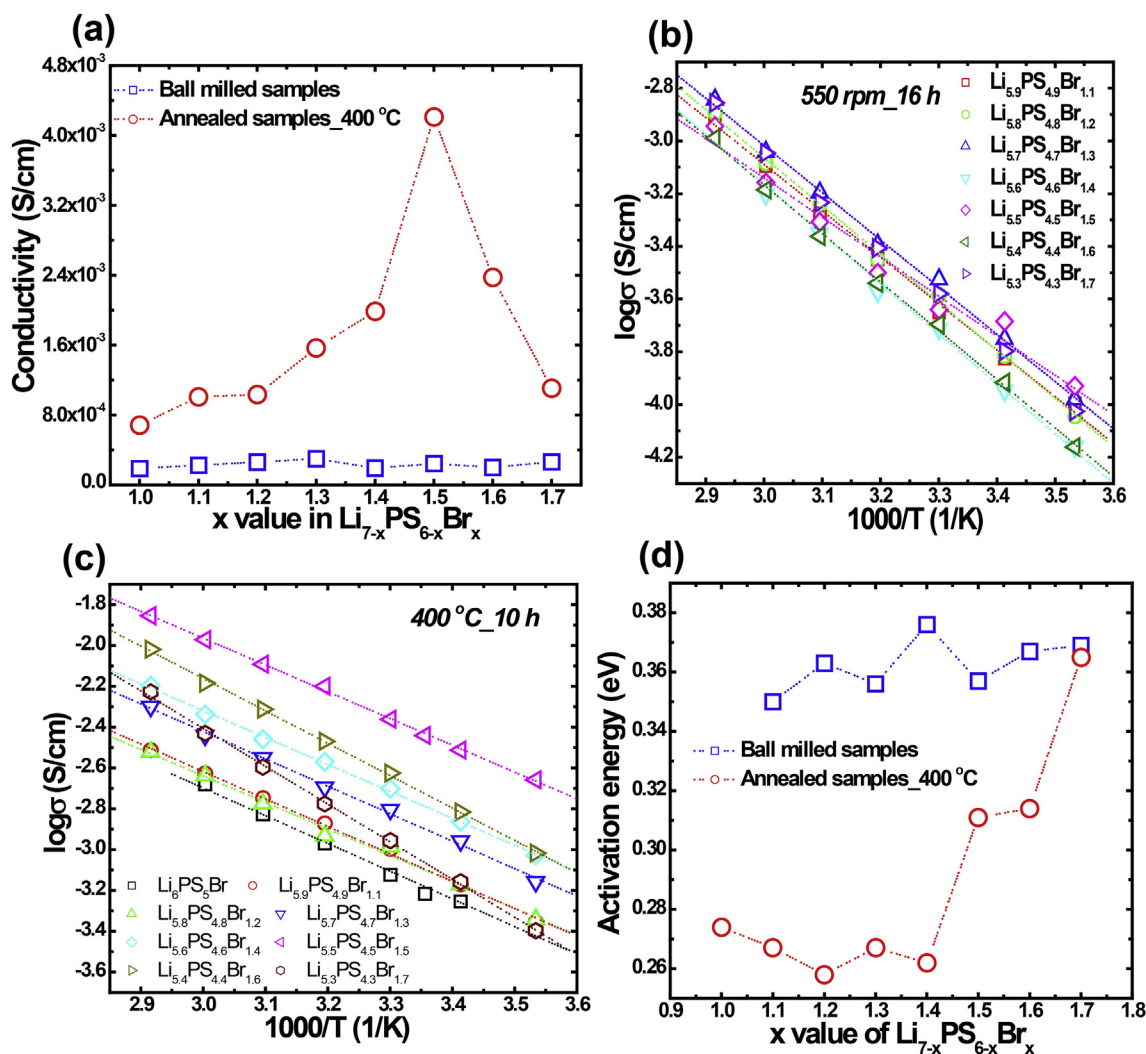


Fig. 2. (a) The lithium ionic conductivity of  $\text{Li}_{7-x}\text{PS}_{6-x}\text{Br}_x$  ( $x = 1.0, 1.1, 1.2, 1.3, 1.4, 1.5, 1.6,$  and  $1.7$ ) obtained from mechanical milling processes (550 rpm/16 h) and heat treatment processes (400 °C/10 h). (b) The corresponding Arrhenius plots of  $\text{Li}_{7-x}\text{PS}_{6-x}\text{Br}_x$  ( $x = 1.1, 1.2, 1.3, 1.4, 1.5, 1.6,$  and  $1.7$ ) obtained from milling processes (550 rpm/16 h). (c) The Arrhenius plots of  $\text{Li}_{7-x}\text{PS}_{6-x}\text{Br}_x$  ( $x = 1.0, 1.1, 1.2, 1.3, 1.4, 1.5, 1.6,$  and  $1.7$ ) annealed at 400 °C for 10 h. (d) The activation energies changes of ball milled and annealed  $\text{Li}_{7-x}\text{PS}_{6-x}\text{Br}_x$  ( $x = 1.0, 1.1, 1.2, 1.3, 1.4, 1.5, 1.6,$  and  $1.7$ ).

lithium ion diffusion.

To systematically investigate the replacement amount of Br in the  $\text{Li}_6\text{PS}_5\text{Br}$ ,  $\text{Li}_{6-x}\text{PS}_{5-x}\text{Br}_x$  ( $x = 1.0\text{--}1.7$ ) was milled and annealed at  $400^\circ\text{C}$  for 10 h. The XRD patterns of  $\text{Li}_{6-x}\text{PS}_{5-x}\text{Br}_x$  ( $x = 1.0\text{--}1.7$ ) obtained after annealing are shown in Figure S1. The major diffraction peaks of all samples can be indexed to the cubic  $F\text{-}43m$  structure, suggesting that the pure lithium argyrodite was obtained for  $\text{Li}_{6-x}\text{PS}_{5-x}\text{Br}_x$  ( $x = 1.0\text{--}1.7$ ). It should be mentioned that very weak reflections originating from  $\text{Li}_2\text{S}$  are still visible at  $27^\circ$  in these patterns. As shown in Fig. 2a, the ball-milled mixtures display much lower room temperature lithium ionic conductivity than the annealed samples. The room temperature lithium ion conductivities of mechanical milled  $\text{Li}_{6-x}\text{PS}_{5-x}\text{Br}_x$  ( $x = 1.0\text{--}1.7$ ) are  $2.25 \times 10^{-4}$  S/cm for  $x = 1.1$ ,  $2.61 \times 10^{-4}$  S/cm for  $x = 1.2$ ,  $2.99 \times 10^{-4}$  S/cm for  $x = 1.3$ ,  $1.94 \times 10^{-4}$  S/cm for  $x = 1.4$ ,  $2.43 \times 10^{-4}$  S/cm for  $x = 1.5$ ,  $2.01 \times 10^{-4}$  S/cm for  $x = 1.6$ , and  $2.64 \times 10^{-4}$  S/cm for  $x = 1.7$ , respectively. After the  $400^\circ\text{C}/10\text{ h}$  annealing processes, the lithium ion conductivities are highly improved. The corresponding lithium ion conductivities are  $1.01 \times 10^{-3}$  S/cm for  $x = 1.1$ ,  $1.03 \times 10^{-3}$  S/cm for  $x = 1.2$ ,  $1.57 \times 10^{-3}$  S/cm for  $x = 1.3$ ,  $1.99 \times 10^{-3}$  S/cm for  $x = 1.4$ ,  $3.76 \times 10^{-3}$  S/cm for  $x = 1.5$ ,  $2.37 \times 10^{-3}$  S/cm for  $x = 1.6$ , and  $1.11 \times 10^{-3}$  S/cm for  $x = 1.7$ , respectively. The differences of lithium ion conductivity for the ball-milled  $\text{Li}_{6-x}\text{PS}_{5-x}\text{Br}_x$  ( $x = 1.0\text{--}1.7$ ) precursors are quite small, which also can be confirmed by the temperature-dependent impedance spectra results as shown in Fig. 2b. However, there are big differences among the ionic conductivities for these annealed  $\text{Li}_{6-x}\text{PS}_{5-x}\text{Br}_x$  ( $x = 1.0\text{--}1.7$ ) samples.  $\text{Li}_{5.5}\text{PS}_{4.5}\text{Br}_{1.5}$  displays the high lithium ion conductivities not only at room temperature (Fig. 2a), but also at any other measuring temperatures (Fig. 2c). To clarify the optimal composition with the highest lithium ion conductivity, these milled  $\text{Li}_{6-x}\text{PS}_{5-x}\text{Br}_x$  ( $x = 1.0\text{--}1.7$ ) precursors were annealed at  $350^\circ\text{C}$  for 10 h and performed by impedance spectroscopy, the room temperature conductivities of which are deduced and shown in Figure S2. The lithium ion conductivities are  $7.37 \times 10^{-4}$  S/cm for  $x = 1$ ,  $8.59 \times 10^{-4}$  S/cm for  $x = 1.1$ ,  $8.74 \times 10^{-4}$  S/cm for  $x = 1.2$ ,  $1.58 \times 10^{-3}$  S/cm for  $x = 1.3$ ,  $2.63 \times 10^{-3}$  S/cm for  $x = 1.4$ ,  $3.27 \times 10^{-3}$  S/cm for  $x = 1.5$ ,  $2.72 \times 10^{-3}$  S/cm for  $x = 1.6$ , and  $1.80 \times 10^{-3}$  S/cm for  $x = 1.7$ , respectively. These results once again confirm that  $\text{Li}_{5.5}\text{PS}_{4.5}\text{Br}_{1.5}$  is the optimal composition with the highest ionic conductivity. The enhanced ionic conductivity of  $\text{Li}_{6-x}\text{PS}_{5-x}\text{Br}_x$  ( $x = 1.0\text{--}1.7$ ) after annealing compared to these milled precursors are due to the decreased activation energies as shown in Fig. 2d. The activation energy differences between the milled and annealed samples decrease with an increase of the Br amount. Since  $\text{Li}_{5.5}\text{PS}_{4.5}\text{Br}_{1.5}$  annealed at  $400^\circ\text{C}$  for 10 h shows the highest lithium ion conductivity, it was chosen as the electrolyte for solid-state batteries in this work. As shown in Figure S3,  $\text{Li}_{5.5}\text{PS}_{4.5}\text{Br}_{1.5}$  annealed at  $400^\circ\text{C}$  for 10 h shows a much smaller particle size than that of  $\text{Li}_6\text{PS}_5\text{Br}$  annealed at  $550^\circ\text{C}$  for 5 h, which is also good for achieving higher lithium ion conductivity. The Raman spectra of  $\text{Li}_6\text{PS}_5\text{Br}$  and  $\text{Li}_{5.5}\text{PS}_{4.5}\text{Br}_{1.5}$  show strong peaks at  $\sim 423\text{ cm}^{-1}$ , weak peaks at  $275\text{ cm}^{-1}$  and  $575\text{ cm}^{-1}$ , as shown in Figure S4, all of which are originating from  $\text{PS}_4^{3-}$  group [36,37]. Previous research has shown that the ionic formula for  $\text{Li}_6\text{PS}_5\text{Br}$  is  $(\text{Li}^+)_6(\text{PS}_4^{3-})_2\text{Br}^-$  [9]. In the Raman spectra figure, no new peaks are observed after the substitution of S with Br in  $(\text{Li}^+)_6(\text{PS}_4^{3-})_2\text{Br}^-$ . The electronic conductivities of  $\text{Li}_6\text{PS}_5\text{Br}$  and  $\text{Li}_{5.5}\text{PS}_{4.5}\text{Br}_{1.5}$  were characterized using a DC polarization method. As shown in Figure S5, the DC electronic conductivities of  $\text{Li}_6\text{PS}_5\text{Br}$  and  $\text{Li}_{5.5}\text{PS}_{4.5}\text{Br}_{1.5}$  were deduced from the test results based on Ohm's Law and delivered values of  $5.53 \times 10^{-9}$  S/cm and  $1.02 \times 10^{-8}$  S/cm at room temperature, respectively. These electronic conductivities are more than five orders of magnitude lower than the lithium ionic conductivities described in the previous section, suggesting that  $\text{Li}_6\text{PS}_5\text{Br}$  and  $\text{Li}_{5.5}\text{PS}_{4.5}\text{Br}_{1.5}$  are typical ionic conductors.

To investigate the anode compatibility of  $\text{Li}_{5.5}\text{PS}_{4.5}\text{Br}_{1.5}$ , both Li and indium foils are chosen as the blocking electrode and anode materials in the measurements. The interfacial behavior of  $\text{Li}_{5.5}\text{PS}_{4.5}\text{Br}_{1.5}$  with Li and indium anode under no electrochemical potential field was evaluated by monitoring the resistance changes of  $\text{Li}/\text{Li}_{5.5}\text{PS}_{4.5}\text{Br}_{1.5}/\text{Li}$  and  $\text{In}/$

$\text{Li}_{5.5}\text{PS}_{4.5}\text{Br}_{1.5}/\text{In}$  cells as a function of time, as shown in Fig. 3a and Fig. 3b. The impedance plots consist of an arc at the high frequencies, a semicircle in the middle frequencies, and a tail at the low frequencies. Previous research has reported that due to the weak bonding between P and S, the  $\text{Li}/\text{Li}_6\text{PS}_5\text{Cl}$  interface quickly decomposes with the formation of multiple phases, such as  $\text{Li}_2\text{S}$ ,  $\text{Li}_3\text{P}$ ,  $\text{LiCl}$ , and possible  $\text{LiP}$  [28]. These quick decomposition products can form a thin layer between the lithium metal and lithium argyrodite solid electrolyte, which reflects as the semicircle and the flat tail in the impedance plots as shown in Fig. 3a. As shown in Fig. 3a, the arc reflects the resistance of the  $\text{Li}_{5.5}\text{PS}_{4.5}\text{Br}_{1.5}$  solid electrolyte, and the semicircle represents the resistance between the side reaction layer and the solid electrolyte, while the flat tail represents the resistance between Li metal and the side reaction layer. The resistance of  $\text{Li}_{5.5}\text{PS}_{4.5}\text{Br}_{1.5}$  slightly decreases with storage durations, while both the semicircle resistance reflects the interface between the side reaction layer and  $\text{Li}_{5.5}\text{PS}_{4.5}\text{Br}_{1.5}$  electrolyte. The flat tail part represents the resistance of the interface between the side reaction layer and lithium metal slowly increase with increasing storage time, suggesting that the decomposition reaction slowly increase as a function of time due to the existence of the side reaction layer without electrochemical potential field. Indium is a commonly used anode for sulfide-based solid-state batteries [11–13]. When indium was chosen as the blocking electrode, as shown in Fig. 3b, negligible changes of the resistance can be observed as a function of time, suggesting that indium is a good anode candidate for  $\text{Li}_{5.5}\text{PS}_{4.5}\text{Br}_{1.5}$ -based solid-state batteries. However, solid-state battery cycle in a working environment under an electrochemical potential field, which is completely different from the above situation. To investigate the resistance changes under the existence of an electrochemical potential field, the resistance changes as a function of storage durations of  $\text{LiNbO}_3$ -coated  $\text{LiNi}_{0.6}\text{Mn}_{0.2}\text{Co}_{0.2}\text{O}_2/\text{Li}_{5.5}\text{PS}_{4.5}\text{Br}_{1.5}/\text{Li}$  and  $\text{LiNbO}_3$ -coated  $\text{LiNi}_{0.6}\text{Mn}_{0.2}\text{Co}_{0.2}\text{O}_2/\text{Li}_{5.5}\text{PS}_{4.5}\text{Br}_{1.5}/\text{In}$  are performed, as shown in Fig. 3c and d. Fig. 3c shows that the onset point with the  $Z'$  axis doesn't change with storage duration time, indicating that the resistance of the  $\text{Li}_{5.5}\text{PS}_{4.5}\text{Br}_{1.5}$  has minimal changes. The semicircles in the high frequency region show slight changes with storage time, suggesting that the resistance between the side reaction layer and the solid electrolyte is maintained the same during the measuring duration. For the impedance spectrum changes of  $\text{LiNbO}_3$ -coated  $\text{LiNi}_{0.6}\text{Mn}_{0.2}\text{Co}_{0.2}\text{O}_2/\text{Li}_{5.5}\text{PS}_{4.5}\text{Br}_{1.5}/\text{In}$ , as shown in Fig. 3d, a similar impedance spectrum as  $\text{In}/\text{Li}_{5.5}\text{PS}_{4.5}\text{Br}_{1.5}/\text{In}$  is observed, and the resistance stays the same as a function of the storage duration, suggesting that  $\text{Li}_{5.5}\text{PS}_{4.5}\text{Br}_{1.5}$  is stable in all scenarios. To evaluate the interface reaction between lithium metal and  $\text{Li}_{5.5}\text{PS}_{4.5}\text{Br}_{1.5}$  electrolyte, X-ray absorption near edge structure (XANES) spectroscopy has been carried out. As shown in Fig. 3e and f, P K-edge and S K-edge XANES spectra of the bare  $\text{Li}_{5.5}\text{PS}_{4.5}\text{Br}_{1.5}$  and  $\text{Li}_{5.5}\text{PS}_{4.5}\text{Br}_{1.5}$  contacted with lithium metal were acquired using fluorescence yield (FLY) modes [38,39]. The white line, the intense peak at the abruptly rising edge of the P K-edge and S K-edge XANES spectra of the bare  $\text{Li}_{5.5}\text{PS}_{4.5}\text{Br}_{1.5}$  are corresponding to the electron transition from 1s orbitals to the unoccupied electronic states of 3p character in the conduction band. Thus, the energy position of the rising edge corresponds to dipole excitations to the bottom of the conduction band. The features beyond the white line often exhibit oscillations which are modulations of the atomic absorption coefficient in a free atom (monotonic) due to multiple scattering of the photoelectron from the neighboring atoms. Thus, these oscillations in absorption coefficient contain information about the local structure of the absorbing atom and therefore are very sensitive to changes in the local environment. Components present can be easily identified with standards. After contacted with lithium metal, several new peaks can be found in both P K-edge and S K-edge XANES spectra. Firstly, there is one broad peak near the edge position of the P K-edge XANES spectrum with energy shift to lower photon energy, which should be related to the reduction of the valence state of P. This indicates the formation of lithium-phosphorus alloys and the composition might be  $\text{Li}_x\text{P}$  ( $x < 3$ ). Additionally, in the S K-edge spectra, new features belonging to  $\text{Li}_2\text{S}$  came out, compared with the

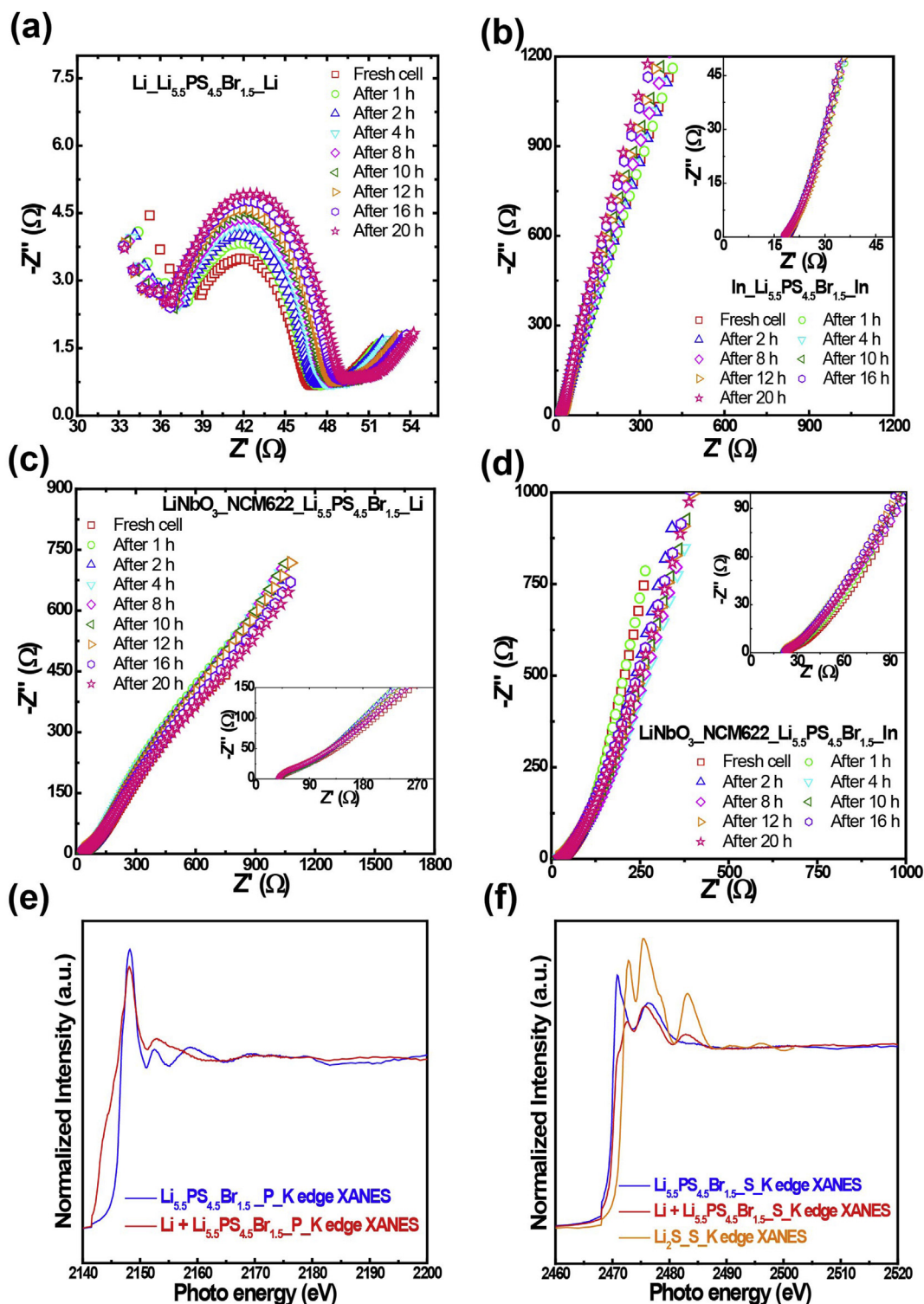


**Fig. 3.** The complex impedance plots of (a)  $\text{Li}/\text{Li}_{5.5}\text{PS}_{4.5}\text{Br}_{1.5}/\text{Li}$  cell, (b)  $\text{In}/\text{Li}_{5.5}\text{PS}_{4.5}\text{Br}_{1.5}/\text{In}$  cell, (c)  $\text{LiNbO}_3\text{-NCM622}/\text{Li}_{5.5}\text{PS}_{4.5}\text{Br}_{1.5}/\text{Li}$  cell, and (d)  $\text{LiNbO}_3\text{-NCM622}/\text{Li}_{5.5}\text{PS}_{4.5}\text{Br}_{1.5}/\text{In}$  cell as a function of storage time. The frequency range was fixed between 7 MHz and 1 Hz with an applied voltage of 0.02 V. The insets in Fig. 3(b–d) show the magnified Nyquist plot of resistance changes as a function of storage time. All measurements were performed at room temperature. (e) P K-edge and (f) S K-edge XANES of the bare  $\text{Li}_{5.5}\text{PS}_{4.5}\text{Br}_{1.5}$  and the  $\text{Li}_{5.5}\text{PS}_{4.5}\text{Br}_{1.5}$  attached with lithium metal. The S K-edge XANES of  $\text{Li}_2\text{S}$  is also shown in Fig. 3f for comparison.

reference spectra. The new features indicate that  $\text{Li}_2\text{S}$  is also formed at the interface, which forms a mixed ionic conductive interface with  $\text{Li}_x\text{P}$  ( $x < 3$ ) together when  $\text{Li}_{5.5}\text{PS}_{4.5}\text{Br}_{1.5}$  contact with lithium metal [38,39].

The stability of  $\text{Li}_6\text{PS}_5\text{Br}$  and  $\text{Li}_{5.5}\text{PS}_{4.5}\text{Br}_{1.5}$  electrolytes against Li was evaluated using a symmetric  $\text{Li}/\text{solid electrolyte}/\text{Li}$  cell at room

temperature. For this kind of measurement, lithium ions are plated/stripped on the surface of the lithium metal electrode. The  $\text{Li}_6\text{PS}_5\text{Br}$  and  $\text{Li}_{5.5}\text{PS}_{4.5}\text{Br}_{1.5}$  electrolytes were pelleted and sandwiched between two pieces of lithium metal foils followed by sealing in model cells, respectively. Fig. 4a shows the polarization of the  $\text{Li}/\text{Li}_6\text{PS}_5\text{Br}/\text{Li}$  cell as a

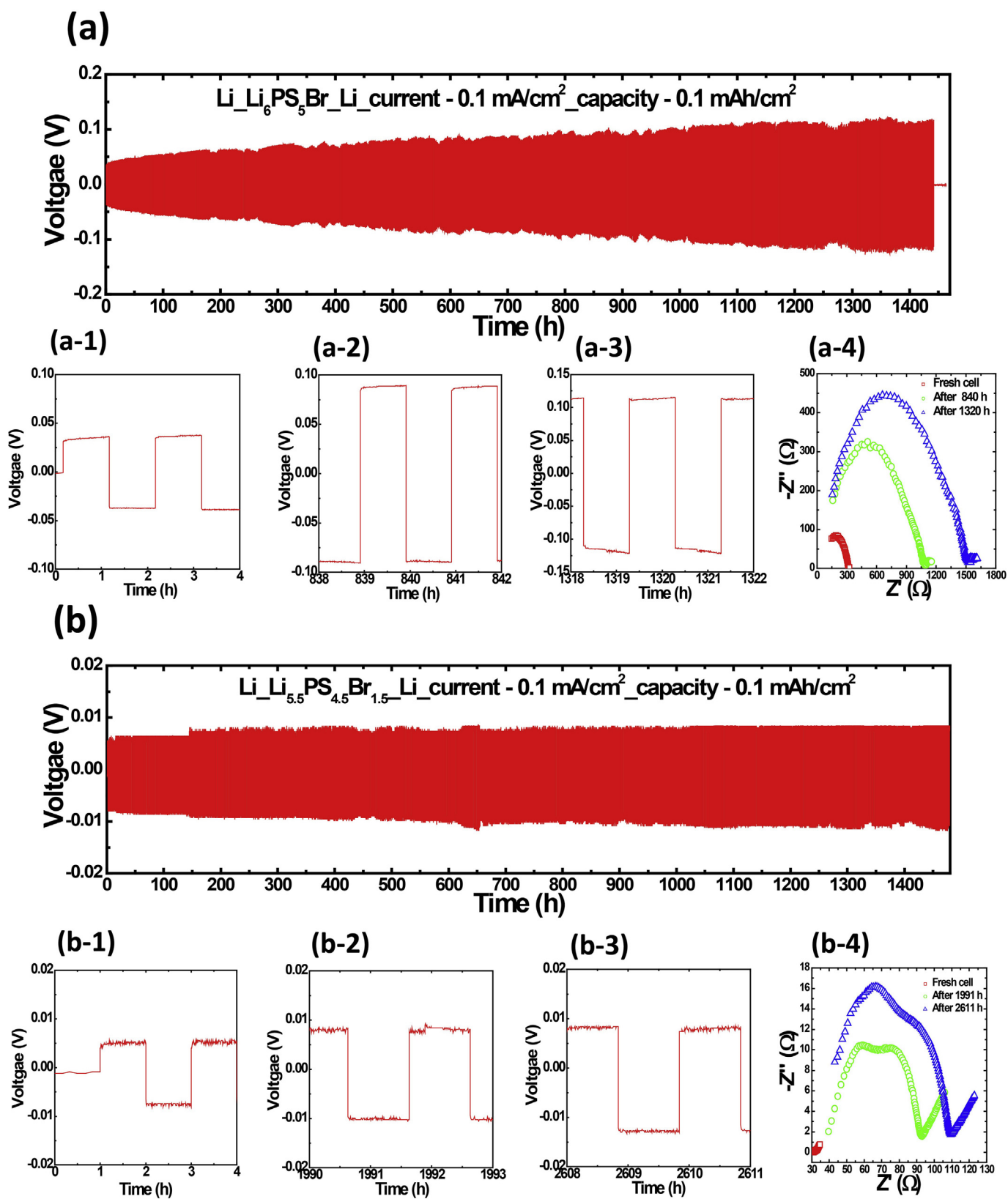


Fig. 4. Electrochemical behavior of (a) the Li/Li<sub>6</sub>PS<sub>5</sub>Br/Li cell and (b) the Li/Li<sub>5.5</sub>PS<sub>4.5</sub>Br<sub>1.5</sub>/Li symmetrical cell under a density of 0.1 mA/cm<sup>2</sup> for 0.1 mA h/cm<sup>2</sup>. (a-1), (a-2), (a-3), (b-1), (b-2), and (b-3) are the magnified regions of the voltage profiles found in Fig. 4a and b. Fig. 4(a-4) and 4 (b-4) are the impedance spectra of these symmetrical cell after various cycling time. All of these measurements were performed at room temperature.

function of the cycling time over 1470 h at a current density of 0.1 mA/cm<sup>2</sup> with a limited capacity of 0.1 mA h/cm<sup>2</sup> at room temperature. The overpotential of the Li/Li<sub>6</sub>PS<sub>5</sub>Br/Li cell progressively increased from 0.033 V (Figs. 4a–1) for the pristine cell to 0.087 V after 840 h of cycling (Figs. 4a–2), and increased to 0.114 V after 1320 h of cycling (Figs. 4a–3). The cell subsequently short circuited after 1370 h (Fig. 4a). Fig. 4a– shows the changes of resistance of the Li/Li<sub>6</sub>PS<sub>5</sub>Br/Li cell during cycling. The depressed semicircles in the lower frequency range represent the interfacial impedance between the Li<sub>6</sub>PS<sub>5</sub>Br electrolyte and lithium metal foil during cycling. The resistance increased with cycling time, from almost 300 Ω for the pristine cell to ~1500 Ω after 1320 h,

suggesting significant side reactions between Li<sub>6</sub>PS<sub>5</sub>Br electrolyte and Li foil. The increased resistance is also reflected by the increase of voltage for the cell as a function of cycling time, as shown in Fig. 4a. A long cycling time of the Li/Li<sub>5.5</sub>PS<sub>4.5</sub>Br<sub>1.5</sub>/Li cell is also performed and shown in Figure S6. For the Li/Li<sub>5.5</sub>PS<sub>4.5</sub>Br<sub>1.5</sub>/Li cell, the overpotential slightly increased from 0.005 V for the pristine cell (Figs. 4b–1) to 0.010 V after 1991 h (Figs. 4b–2), to 0.013 V after 2611 h (Figs. 4b–3). The resistance increased at a slower rate compared to that of the Li/Li<sub>6</sub>PS<sub>5</sub>Br/Li cell as shown in Fig. 4b–. There are two arcs in the impedance spectra of the Li/Li<sub>5.5</sub>PS<sub>4.5</sub>Br<sub>1.5</sub>/Li cell. It should be mentioned that due to the lower resistance of the Li/Li<sub>5.5</sub>PS<sub>4.5</sub>Br<sub>1.5</sub>/Li cell compared to that of the Li/

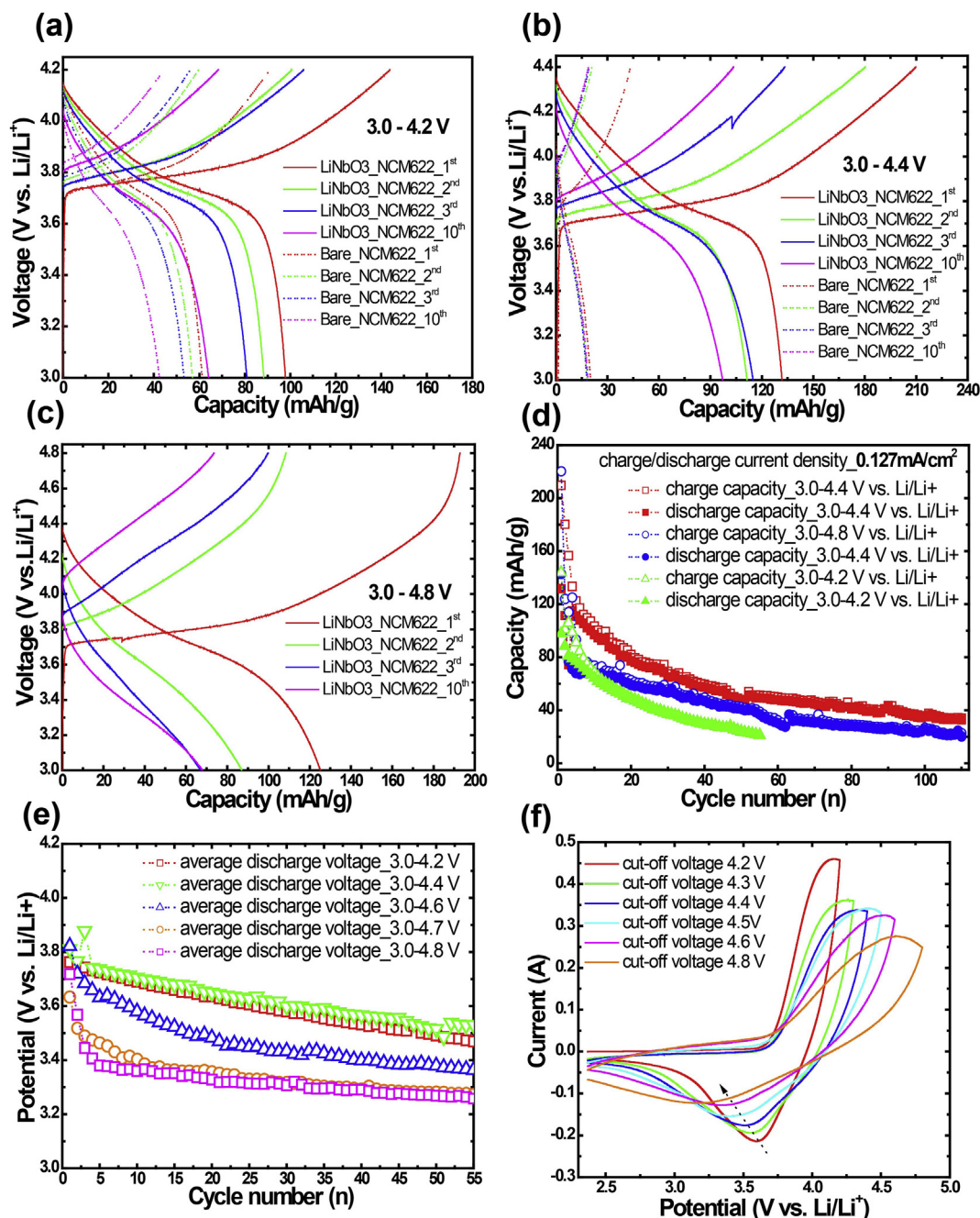


Fig. 5. The charge/discharge galvanostatic voltage curves for the assembled Bare-NCM622/Li<sub>5.5</sub>PS<sub>4.5</sub>Br<sub>1.5</sub>/Li and LiNbO<sub>3</sub>-NCM622/Li<sub>5.5</sub>PS<sub>4.5</sub>Br<sub>1.5</sub>/Li solid-state batteries under different cut-off voltages, which cycled (a) between 3.0 and 4.2 V, (b) between 3.0 and 4.4 V, and (c) between 3.0 and 4.8 V vs. Li/Li<sup>+</sup>. The charge/discharge current density is fixed at 0.127 mA/cm<sup>2</sup>. (d) The corresponding charge/discharge capacity retention as a function of cycling number under different cut-off voltage windows. (e) The changes of the average discharge voltage under different cut-off voltages with increasing cycling number. (f) The cyclic voltammograms of the LiNbO<sub>3</sub>-LiNi<sub>0.6</sub>Mn<sub>0.2</sub>Co<sub>0.2</sub>O<sub>2</sub>/Li<sub>5.5</sub>PS<sub>4.5</sub>Br<sub>1.5</sub>/Li solid-state batteries for different upper cut-off voltages at a scanning rate of 0.1 mV/s. All of these measurements were performed at room temperature.

Li<sub>6</sub>PS<sub>5</sub>Br/Li cell, the two arcs clearer in Fig. 4b–. The Li/Li<sub>5.5</sub>PS<sub>4.5</sub>Br<sub>1.5</sub>/Li symmetric cell shows a much longer cycling life than that of the Li/Li<sub>6</sub>PS<sub>5</sub>Br/Li cell, suggesting Li<sub>5.5</sub>PS<sub>4.5</sub>Br<sub>1.5</sub> has better stability against Li foil. When the cycling current density and the limited capacity separately increased to higher values, such as 0.5 mA/cm<sup>2</sup> and 0.5 mA h/cm<sup>2</sup> (Figure S7a and Figure S7b, respectively), the Li/Li<sub>6</sub>PS<sub>5</sub>Br/Li cell displays reversible plating/stripping behavior, although the voltage of which increased with an increase of cycling time. More importantly, when both the current density and the capacity increased to higher values, such as 0.2 mA/cm<sup>2</sup> and 0.2 mA h/cm<sup>2</sup>, the Li/Li<sub>5.5</sub>PS<sub>4.5</sub>Br<sub>1.5</sub>/Li exhibits stable cycling behaviors even after 800 h with extremely slowly increase of the voltages, as shown in Figure S7c. The above symmetric cell results for the Li<sub>5.5</sub>PS<sub>4.5</sub>Br<sub>1.5</sub> solid electrolyte show that although there are side reactions between Li foil and Li<sub>5.5</sub>PS<sub>4.5</sub>Br<sub>1.5</sub>, a long cycle life for Li<sub>5.5</sub>PS<sub>4.5</sub>Br<sub>1.5</sub>-based solid-state Li metal battery is possible.

The above Li/Li<sub>5.5</sub>PS<sub>4.5</sub>Br<sub>1.5</sub>/Li symmetrical cell results implied that Li has the potential to be an anode material for Li<sub>5.5</sub>PS<sub>4.5</sub>Br<sub>1.5</sub>-based solid-state batteries. To clarify the possibility of long cycle life for Li<sub>5.5</sub>PS<sub>4.5</sub>Br<sub>1.5</sub>-based solid-state Li metal batteries, solid-state batteries using Li<sub>5.5</sub>PS<sub>4.5</sub>Br<sub>1.5</sub> solid electrolyte in a combination with the bare NCM622 or LiNbO<sub>3</sub>-coated LiNi<sub>0.6</sub>Mn<sub>0.2</sub>Co<sub>0.2</sub>O<sub>2</sub> cathodes and Li metal anodes. The cells were assembled and cycled under various upper cut-off voltages (4.2, 4.4, and 4.8 V vs. Li/Li<sup>+</sup>) with the current density of 0.127 mA/cm<sup>2</sup> (~0.1C). Fig. 5(a–c) shows the initial, second, third, and the tenth charge/discharge profiles of bare LiNi<sub>0.6</sub>Mn<sub>0.2</sub>Co<sub>0.2</sub>O<sub>2</sub>/Li<sub>5.5</sub>PS<sub>4.5</sub>Br<sub>1.5</sub>/Li and LiNbO<sub>3</sub>-coated LiNi<sub>0.6</sub>Mn<sub>0.2</sub>Co<sub>0.2</sub>O<sub>2</sub>/Li<sub>5.5</sub>PS<sub>4.5</sub>Br<sub>1.5</sub>/Li solid-state batteries cycled at various upper cut-off voltages (4.2, 4.4 V, and 4.8 V vs. Li/Li<sup>+</sup>) and a fixed discharge cut-off voltage of 3.0 V vs. Li/Li<sup>+</sup>. When the upper cut-off voltage is 4.2 or 4.4 V vs. Li/Li<sup>+</sup>, typical charge/discharge plateaus are observed in Fig. 5a and b. However, when the charge cut-off voltage is increased to 4.8 V vs. Li/Li<sup>+</sup>, the charge-discharge profiles display much larger voltage polarization compared to the aforementioned cases. The typical charge/discharge plateaus corresponding to LiNi<sub>0.6</sub>Mn<sub>0.2</sub>Co<sub>0.2</sub>O<sub>2</sub> disappear when the upper cut-off voltage increases. It appears that the polarization of Li<sub>5.5</sub>PS<sub>4.5</sub>Br<sub>1.5</sub>-based solid-state batteries are highly dependent on the upper cut-off voltage, and increase with higher cut-off voltages. The initial charge and discharge capacities of the solid-state battery using the bare NCM622 under the upper cut-off voltage of 4.2 V vs. Li/Li<sup>+</sup> were 90.9 and 61.2 mA h/g when the charge/discharge current density was fixed at 0.127 mA/cm<sup>2</sup> (~0.1C). After coating NCM622 with a homogeneous layer of LiNbO<sub>3</sub> using ALD, the initial charge and discharge capacities of this electrode increased to 143.8 and 97.9 mA h/g, respectively. After coating, the initial Coulombic efficiency for the NCM622 electrode slightly increased, from 67.39% to 68.08% under this cycle window. When the upper cut-off voltage increases to 4.4 V vs. Li/Li<sup>+</sup>, the initial charge and discharge capacities of the bare NCM622 electrode were 43.3 and 20.2 mA h/g with a coulombic efficiency of 46.69%, while the corresponding capacities for the LiNbO<sub>3</sub>-coated NCM622 electrode were 209.7 and 131.8 mA h/g and the coulombic efficiency was 62.84%, respectively. It can be seen that the LiNbO<sub>3</sub> coating layer can not only enhance the charge/discharge capacity of Li<sub>5.5</sub>PS<sub>4.5</sub>Br<sub>1.5</sub>-based solid-state Li metal batteries, but also can improve the initial Coulombic efficiency, especially at higher cut-off voltages. Due to the high reactivity of Li<sub>5.5</sub>PS<sub>4.5</sub>Br<sub>1.5</sub> with the bare LiMn<sub>x</sub>Ni<sub>y</sub>Co<sub>z</sub>O<sub>2</sub> (x + y + z = 1) at higher cut-off voltages, the corresponding Li<sub>5.5</sub>PS<sub>4.5</sub>Br<sub>1.5</sub>-based solid-state Li metal showed poor electrochemical. The homogeneously-coated LiNbO<sub>3</sub> layer can impede the direct contact between the Li<sub>5.5</sub>PS<sub>4.5</sub>Br<sub>1.5</sub> layer and the active material, thus inhibiting side reactions and improving the electrochemical performances. When the upper charge cut-off voltage increases up to 4.8 V, the initial charge and discharge capacities were 220.3 and 143.0 mA h/g, respectively. The charge capacities of the LiNbO<sub>3</sub>-coated LiNi<sub>0.6</sub>Mn<sub>0.2</sub>Co<sub>0.2</sub>O<sub>2</sub>/Li<sub>5.5</sub>PS<sub>4.5</sub>Br<sub>1.5</sub>/Li battery are higher than 200 mA h/g when the upper cut-off voltages are set to 4.4 and 4.8 V vs. Li/Li<sup>+</sup>, suggesting that part of the Li<sub>5.5</sub>PS<sub>4.5</sub>Br<sub>1.5</sub> electrolyte in the cathode mixture was decomposed.

Moreover, the initial charge/discharge capacities of LiNbO<sub>3</sub>-coated LiNi<sub>0.6</sub>Mn<sub>0.2</sub>Co<sub>0.2</sub>O<sub>2</sub>/Li<sub>5.5</sub>PS<sub>4.5</sub>Br<sub>1.5</sub>/Li battery increase with the increasing of upper charge cut-off voltages. The discharge capacities are 64.1 mA h/g for 4.2 V, 97.2 mA h/g for 4.4 V, and 68 mA h/g for 4.8 V after 10 cycles, respectively. When Li metal is chosen as the anode materials for the Li<sub>5.5</sub>PS<sub>4.5</sub>Br<sub>1.5</sub>-based solid-state battery, faster capacity decay is observed compared to the cells using In as anode, as shown in Fig. 5a–c and Fig. 6b, which may be associated with the side reaction layer between the lithium metal and Li<sub>5.5</sub>PS<sub>4.5</sub>Br<sub>1.5</sub> solid electrolyte layer. The mobility of Li ions is impeded by this layer, causing a decrease in ionic transport across the interface. Fig. 5d depicts the capacity decay plots of Li<sub>5.5</sub>PS<sub>4.5</sub>Br<sub>1.5</sub>-based lithium metal solid-state battery when cycled under various upper charge cut-off voltages (4.2, 4.4, and 4.8 V vs. Li/Li<sup>+</sup>) at a current density of 0.127 mA/cm<sup>2</sup>. After 55 cycles, the battery delivers discharge capacities of 21 mA h/g at 4.2 V, 49.6 mA h/g at 4.4 V, and 36.9 mA h/g at 4.8 V, respectively, with the corresponding average discharge capacity decay rate of 1.40%, 1.49%, and 1.93%. The average discharge capacity decay rate increases with the increment of the upper charge cut-off voltages. Higher cut-off voltage induces strong degradation of the battery components. A higher voltage may cause irreversible structural changes of the NCM cathode, yielding a capacity fading [40]. Additionally, when the charge voltage is higher than the electrochemical stability window of the solid electrolyte, an irreversible decomposition of the solid electrolyte occurs, causing serious capacity fade of the solid-state batteries. As shown in Fig. 5d, the Li<sub>5.5</sub>PS<sub>4.5</sub>Br<sub>1.5</sub>-based solid-state lithium metal battery can be cycled more than 110 cycles, suggesting that lithium argyrodite-based solid-state lithium metal battery with long cycling life is feasible. For the bare NCM622/Li<sub>5.5</sub>PS<sub>4.5</sub>Br<sub>1.5</sub>/Li battery, as shown in Figure S8, more than 100 cycles can be achieved. Without the LiNbO<sub>3</sub> coating layer to separate the active material and the lithium argyrodite solid electrolyte, solid-state lithium metal batteries can still achieve long cycle life, suggesting that the problem associated with lithium argyrodite-based solid-state lithium metal batteries is associated with the anode side. This is in good agreement with the current research results which claim the possibility of enabling lithium metal anodes in Li<sub>6</sub>PS<sub>5</sub>Cl-based all-solid-state batteries at reasonable stack pressures [41]. Considering the much lower initial discharge capacity when the battery is cycled at 4.2 V compared to 4.4 V, the latter is a better charge/discharge voltage window for Li<sub>5.5</sub>PS<sub>4.5</sub>Br<sub>1.5</sub>-based lithium metal solid-state batteries. This is also confirmed by the changes in the average discharging voltage under different cut-off voltages during cycling, as shown in Fig. 5e. The battery delivers a slightly higher average discharging voltage at 4.4 V compared to 4.2 V, and a much higher average discharging voltage when raising the upper charge cut-off voltages. To confirm this and further unravel the activation effect of various upper cut-off voltages on the polarization behavior of the electrodes, cyclic voltammetry is performed in different voltage windows with a sweep rate of 0.1 mV/s, as shown in Fig. 5f. For a typical lithium ion battery using LiNi<sub>x</sub>Co<sub>y</sub>Mn<sub>z</sub>O<sub>2</sub> (x + y + z = 1) as an active cathode in a combination with organic liquid electrolyte, the oxidation peaks (Ni<sup>2+</sup>/Ni<sup>4+</sup>) and the reduction peaks (Ni<sup>4+</sup>/Ni<sup>2+</sup>) are located at ~4.10 V and ~3.65 V, respectively [42]. When the scan window is raised to a higher voltage, the oxidation peak due to the Ni<sup>2+</sup>/Ni<sup>4+</sup> pair shifts to higher voltage potentials, while the reduction peak due to the Ni<sup>4+</sup>/Ni<sup>2+</sup> pair moves to lower voltage potentials, yielding a larger polarization at wider voltage windows, which is in good agreement with the charge/discharge profiles as shown in Fig. 5a–c. Moreover, the oxidation peak moves to the higher potentials in a wider voltage window, promoting the decomposition of solid electrolyte and side reactions.

The above results have proven that indium foil shows better compatibility with Li<sub>5.5</sub>PS<sub>4.5</sub>Br<sub>1.5</sub> than that of Li metal no matter if there is an electrochemical potential field or not, suggesting that indium is good anode candidate for Li<sub>5.5</sub>PS<sub>4.5</sub>Br<sub>1.5</sub>-based solid-state batteries. Hereby, indium foil was chosen as the anode in combination with the bare and LiNbO<sub>3</sub>-coated LiNi<sub>0.6</sub>Mn<sub>0.2</sub>Co<sub>0.2</sub>O<sub>2</sub> cathode and Li<sub>5.5</sub>PS<sub>4.5</sub>Br<sub>1.5</sub> solid electrolyte. Fig. 6a shows the first five cycles of charge/discharge

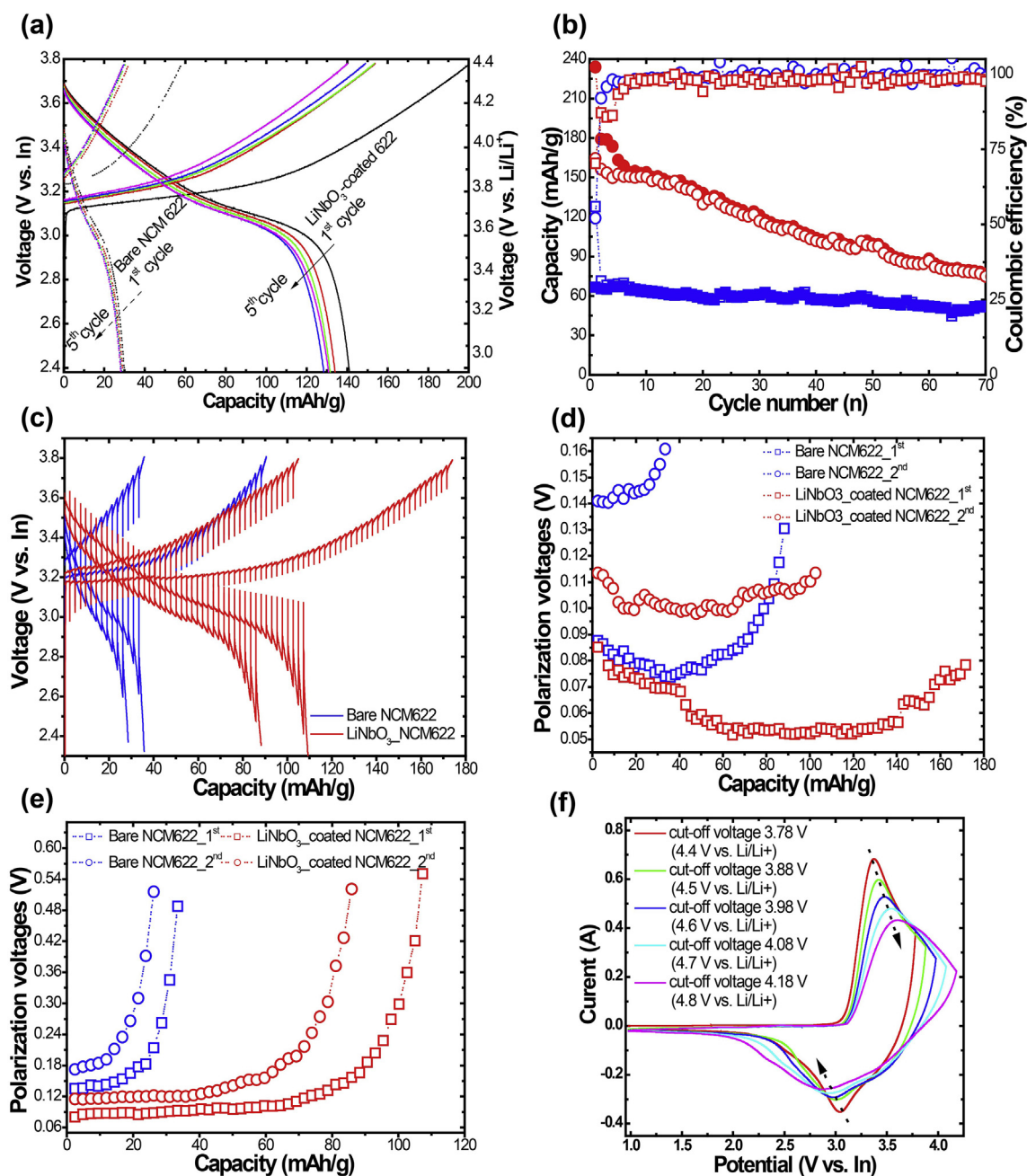


**Fig. 6.** (a) The initial five charge/discharge plots of  $\text{Li}_{5.5}\text{PS}_{4.5}\text{Br}_{1.5}$ -based solid-state battery using  $\text{LiNi}_{0.6}\text{Mn}_{0.2}\text{Co}_{0.2}\text{O}_2$  with and without  $\text{LiNbO}_3$  coating layer in combination with a In anode under the current density of  $0.255 \text{ mA}/\text{cm}^2$  ( $\sim 0.2\text{C}$ ) between 2.38 and 3.78 V vs. In (between 3.0 and 4.4 V vs.  $\text{Li}/\text{Li}^+$ ). (b) The corresponding charge/discharge capacities and Coulombic efficiencies as a function of cycle number. (c) The GITT plots, (d) charge polarization voltages, and (e) discharge polarization voltages during the first two cycles. (f) The CV profiles of  $\text{LiNbO}_3$ -coated  $\text{LiNi}_{0.6}\text{Mn}_{0.2}\text{Co}_{0.2}\text{O}_2/\text{Li}_{5.5}\text{PS}_{4.5}\text{Br}_{1.5}/\text{In}$  scanned under various voltage windows with a rate of  $0.1 \text{ mV}/\text{s}$ . All of these measurements were performed at room temperature.

profiles of solid-state batteries using the bare  $\text{LiNi}_{0.6}\text{Mn}_{0.2}\text{Co}_{0.2}\text{O}_2$  cathode and  $\text{LiNbO}_3$ -coated  $\text{LiNi}_{0.6}\text{Mn}_{0.2}\text{Co}_{0.2}\text{O}_2$  cathode at the current density of  $0.255 \text{ mA}/\text{cm}^2$  ( $\sim 0.2\text{C}$ ) between 2.38 and 3.78 V vs. In (3.0–4.4 V vs.  $\text{Li}/\text{Li}^+$ ). The initial charge and discharge capacities of the bare  $\text{LiNi}_{0.6}\text{Mn}_{0.2}\text{Co}_{0.2}\text{O}_2$  cathode were 58.3 and 29.9 mA h/g with a Coulombic efficiency of 51.4%, while the corresponding capacities for the  $\text{LiNbO}_3$ -coated  $\text{LiNi}_{0.6}\text{Mn}_{0.2}\text{Co}_{0.2}\text{O}_2$  cathode were 234.0 and 164.6 mA h/g with a coulombic efficiency of 70.35%, respectively. The bare  $\text{LiNi}_{0.6}\text{Mn}_{0.2}\text{Co}_{0.2}\text{O}_2$  is unstable with the  $\text{Li}_{5.5}\text{PS}_{4.5}\text{Br}_{1.5}$  electrolyte in the cathode mixture and will react with the active material to yield lower capacities and Coulombic efficiency. However, both the charge/discharge capacities and the coulombic efficiency are improved due to

the introduction of the  $\text{LiNbO}_3$  coating layer. The homogeneously coated  $\text{LiNbO}_3$  with ALD can isolate the  $\text{LiNi}_{0.6}\text{Mn}_{0.2}\text{Co}_{0.2}\text{O}_2$  active materials from the  $\text{Li}_{5.5}\text{PS}_{4.5}\text{Br}_{1.5}$  electrolyte and thus impede the side reactions at the interface. The extremely high initial charge capacity (234 mA h/g) of the  $\text{LiNbO}_3$ -coated  $\text{LiNi}_{0.6}\text{Mn}_{0.2}\text{Co}_{0.2}\text{O}_2$  cathode suggests that part of the  $\text{Li}_{5.5}\text{PS}_{4.5}\text{Br}_{1.5}$  decomposes during the initial charge processing and not all of these decomposition products are reversible in the subsequent charge/discharge cycles. After 45 charge/discharge cycles, the bare  $\text{LiNi}_{0.6}\text{Mn}_{0.2}\text{Co}_{0.2}\text{O}_2$  cathode delivered a discharge capacity of 25.7 mA h/g. In contrast, the discharge capacity of the  $\text{LiNbO}_3$ -coated  $\text{LiNi}_{0.6}\text{Mn}_{0.2}\text{Co}_{0.2}\text{O}_2$  cathode was 98.4 mA h/g, and maintained a discharge capacity of 74.9 mA h/g after 70 cycles, as shown in Fig. 6b.

Galvanostatic intermittent titration technique (GITT) was performed on both the bare  $\text{LiNi}_{0.6}\text{Mn}_{0.2}\text{Co}_{0.2}\text{O}_2$  and the  $\text{LiNbO}_3$ -coated  $\text{LiNi}_{0.6}\text{Mn}_{0.2}\text{Co}_{0.2}\text{O}_2$  electrodes to unravel the influence of the coating layer on the polarization effect in solid-state batteries. The transient charge/discharge profiles of the first two cycles for solid-state batteries using the bare  $\text{LiNi}_{0.6}\text{Mn}_{0.2}\text{Co}_{0.2}\text{O}_2$  and the  $\text{LiNbO}_3$ -coated  $\text{LiNi}_{0.6}\text{Mn}_{0.2}\text{Co}_{0.2}\text{O}_2$  cathodes as active materials when cycled at 0.1C are shown in Fig. 6c. The  $\text{LiNbO}_3$ -coated  $\text{LiNi}_{0.6}\text{Mn}_{0.2}\text{Co}_{0.2}\text{O}_2$  cathode shows much higher discharge capacities than that of the bare  $\text{LiNi}_{0.6}\text{Mn}_{0.2}\text{Co}_{0.2}\text{O}_2$  cathode, which is in good agreement with the results showed in Fig. 6a when these batteries are cycled at a larger rate (0.1C vs. 0.2C). As shown in Fig. 6d and e, the  $\text{LiNbO}_3$ -coated  $\text{LiNi}_{0.6}\text{Mn}_{0.2}\text{Co}_{0.2}\text{O}_2$  cathode delivers much smaller voltage polarizations than that of the bare  $\text{LiNi}_{0.6}\text{Mn}_{0.2}\text{Co}_{0.2}\text{O}_2$  cathode during the first two cycles, indicating that the  $\text{LiNbO}_3$  coating layer can effectively decrease the polarization of  $\text{LiNi}_{0.6}\text{Mn}_{0.2}\text{Co}_{0.2}\text{O}_2$  cathode. To further investigate the activation effect of the upper cut-off voltages on the polarization behavior of the  $\text{LiNbO}_3$ -coated  $\text{LiNi}_{0.6}\text{Mn}_{0.2}\text{Co}_{0.2}\text{O}_2$  cathode, cyclic voltammogram curves of the  $\text{LiNbO}_3$ -coated  $\text{LiNi}_{0.6}\text{Mn}_{0.2}\text{Co}_{0.2}\text{O}_2/\text{Li}_{5.5}\text{PS}_{4.5}\text{Br}_{1.5}/\text{In}$  solid-state batteries under different upper cut-off voltages were recorded at a sweep rate of 0.1 mV/s as shown in Fig. 6f. Unlike the  $\text{LiNbO}_3$ -coated  $\text{LiNi}_{0.6}\text{Mn}_{0.2}\text{Co}_{0.2}\text{O}_2$  cathode using Li metal anode showed in Fig. 5f, a clear pair of oxidation peaks at  $\sim 3.27$  V vs. In and a reduction peak at  $\sim 3.08$  V vs. In is observed in Fig. 6f, which corresponds to the oxidation and reduction processes of  $\text{Ni}^{2+}/\text{Ni}^{4+}$  followed by the oxidation process of  $\text{Co}^{3+}/\text{Co}^{4+}$ , respectively. As shown in the figure, the position of the reduction peak at  $\sim 3.08$  V vs. In shifts towards the lower potentials with the increased upper cut-off voltages, while the position of the oxidation peak at  $\sim 3.27$  V slightly shifts to the higher potentials. The differences between this pair of reduction and oxidation peaks became larger with increasing cut-off voltages, suggesting the increase of the polarization effect with the increment of the cut-off voltages. Moreover, there are weak peaks locate at  $\sim 3.58$  V vs. In during the reduction processes at various voltage windows, which may be caused by the side reaction between  $\text{Ni}^{4+}$  and the  $\text{Li}_{5.5}\text{PS}_{4.5}\text{Br}_{1.5}$  solid electrolyte.

#### 4. Conclusions

In summary, the lithium ion conductivity of  $\text{Li}_6\text{PS}_5\text{Br}$  was enhanced by replacing S with Br and the optimal composition of  $\text{Li}_{5.5}\text{PS}_{4.5}\text{Br}_{1.5}$  was optimized with a room temperature conductivity of  $4.35 \times 10^{-3} \text{ S/cm}$ .  $^7\text{Li}$  SLR NMR and AIMD simulations results have confirmed that the improvement of lithium ion conductivity was due to the decrease of the energy barrier for local lithium ion jumps after the substitution of S with Br. The introduction of Br not only increased the ionic conductivity but also improved lithium compatibility. The stable cycle behavior and small changes of resistance for  $\text{Li}/\text{Li}_{5.5}\text{PS}_{4.5}\text{Br}_{1.5}/\text{Li}$  cell provided the possibility to assemble  $\text{Li}_{5.5}\text{PS}_{4.5}\text{Br}_{1.5}$ -based solid-state Li metal batteries with a long cycling life. The better chemical stability between In and  $\text{Li}_{5.5}\text{PS}_{4.5}\text{Br}_{1.5}$  compared to that with Li metal made indium foil a better anode material for  $\text{Li}_{5.5}\text{PS}_{4.5}\text{Br}_{1.5}$ -based solid-state batteries, yielding higher capacity and better cyclability.

#### Declaration of competing interest

The authors declare that they have no known competing financial interests or personal relationships that could have appeared to influence the work reported in this paper.

#### CRedit authorship contribution statement

**Chuang Yu:** Conceptualization, Formal analysis, Investigation, Writing - original draft. **Yong Li:** Writing - original draft. **Weihan Li:** Writing - original draft. **Keegan R. Adair:** Writing - original draft. **Feipeng Zhao:** Writing - original draft. **Mathew Willans:** Writing - original draft. **Jianwen Liang:** Writing - original draft. **Yang Zhao:** Writing -

original draft. **Changhong Wang:** Writing - original draft. **Sixu Deng:** Writing - original draft. **Ruying Li:** Writing - original draft. **Huan Huang:** Writing - original draft. **Shigang Lu:** Writing - original draft. **Tsun-Kong Sham:** Writing - original draft. **Yining Huang:** Writing - original draft, Supervision. **Xueliang Sun:** Writing - original draft, Formal analysis, Supervision.

#### Acknowledgments

This work was supported by Natural Sciences and Engineering Research Council of Canada (NSERC), Canada Research Chair Program (CRC), Ontario Research Fund (ORF), GLABAT Solid-State Battery Inc., China Automotive Battery Research Institute, Canada Foundation of Innovation (CFI), and The University of Western Ontario. This work was also funded by the Canada Light Source (CLS) at the University of Saskatchewan. We also appreciate the help of the beamline scientists of Soft X-ray microcharacterization beamline beamline (SXRMB) at Canadian Light Source, Dr. Yongfeng Hu and Dr. Qunfeng Xiao.

#### Appendix A. Supplementary data

Supplementary data related to this article can be found at <https://doi.org/10.1016/j.ensm.2020.04.014>.

#### References

- [1] E. Quartarone, P. Mustarelli, Electrolytes for solid-state lithium rechargeable batteries: recent advances and perspectives, *Chem. Soc. Rev.* 40 (2011) 2525–2540.
- [2] J.B. Goodenough, How we made the Li-ion rechargeable battery, *Nat. Electronics* 1 (2018) 204.
- [3] W. An, B. Gao, S. Mei, B. Xiang, J. Fu, L. Wang, Q. Zhang, P.K. Chu, K. Huo, Scalable synthesis of ant-nest-like bulk porous silicon for high-performance lithium-ion battery anodes, *Nat. Commun.* 10 (2019) 1–11.
- [4] Z. Zheng, P. Li, J. Huang, H. Liu, Y. Zao, Z. Hu, L. Zhang, H. Chen, M.-S. Wang, D.-L. Peng, High performance columnar-like  $\text{Fe}_2\text{O}_3$ @ carbon composite anode via yolk@ shell structural design, *J. Energy Chem.* 41 (2020) 126–134.
- [5] L. Lu, X. Han, J. Li, J. Hua, M. Ouyang, A review on the key issues for lithium-ion battery management in electric vehicles, *J. Power Sources* 226 (2013) 272–288.
- [6] Z. Gao, H. Sun, L. Fu, F. Ye, Y. Zhang, W. Luo, Y. Huang, Promises, challenges, and recent progress of inorganic solid-state electrolytes for all-solid-state lithium batteries, *Adv. Mater.* 30 (2018) 1705702.
- [7] J. Liang, J. Luo, Q. Sun, X. Yang, R. Li, X. Sun, Recent progress on solid-state hybrid electrolytes for solid-state lithium batteries, *Energy Stor. Mater.* 21 (2019) 308–334.
- [8] J. Janek, W.G. Zeier, A solid future for battery development, *Nat. Energy* 1 (2016) 16141.
- [9] H.J. Deiseroth, S.T. Kong, H. Eckert, J. Vannahme, C. Reiner, T. Zais, M. Schlosser,  $\text{Li}_6\text{PS}_5\text{X}$ : a class of crystalline Li-rich solids with an unusually high  $\text{Li}^+$  mobility, *Angew. Chem. Int. Ed.* 47 (2008) 755–758.
- [10] C. Yu, S. Ganapathy, N.J.J. de Klerk, I. Roslon, E.R.H. van Eck, A.P.M. Kentgens, M. Wagemaker, Unravelling Li-ion transport from picoseconds to seconds: bulk versus interfaces in an argyrodite  $\text{Li}_6\text{PS}_5\text{Cl}-\text{Li}_2\text{S}$  all-solid-state Li-ion battery, *J. Am. Chem. Soc.* 138 (2016) 11192–11201.
- [11] C. Yu, S. Ganapathy, J. Hageman, L. van Eijck, E.R. van Eck, L. Zhang, T. Schwietert, S. Basak, E.M. Kelder, M. Wagemaker, Facile synthesis toward the optimal structure-conductivity characteristics of the argyrodite  $\text{Li}_6\text{PS}_5\text{Cl}$  solid-state electrolyte, *ACS Appl. Mater. Interfaces* 10 (2018) 33296–33306.
- [12] C. Yu, S. Ganapathy, E.R.H. van Eck, L. van Eijck, S. Basak, Y. Liu, L. Zhang, H. Zandbergen, M. Wagemaker, Revealing the relation between the structure, Li-ion conductivity and solid-state battery performance of the argyrodite  $\text{Li}_6\text{PS}_5\text{Br}$  solid electrolyte, *J. Mater. Chem. A* 5 (2017) 21178–21188.
- [13] C. Yu, L. van Eijck, S. Ganapathy, M. Wagemaker, Synthesis, structure and electrochemical performance of the argyrodite  $\text{Li}_6\text{PS}_5\text{Cl}$  solid electrolyte for Li-ion solid state batteries, *Electrochim. Acta* 215 (2016) 93–99.
- [14] S. Boulineau, M. Courty, J.-M. Tarascon, V. Viallet, Mechanochemical synthesis of Li-argyrodite  $\text{Li}_6\text{PS}_5\text{X}$  (X = Cl, Br, I) as sulfur-based solid electrolytes for all solid state batteries application, *Solid State Ionics* 221 (2012) 1–5.
- [15] R.P. Rao, S. Adams, Studies of lithium argyrodite solid electrolytes for all-solid-state batteries, *Phys. Status Solidi* 208 (2011) 1804–1807.
- [16] R.P. Rao, N. Sharma, V. Peterson, S. Adams, Formation and conductivity studies of lithium argyrodite solid electrolytes using in-situ neutron diffraction, *Solid State Ionics* 230 (2013) 72–76.
- [17] C. Yu, S. Ganapathy, E.R. Van Eck, H. Wang, S. Basak, Z. Li, M. Wagemaker, Accessing the bottleneck in all-solid state batteries, lithium-ion transport over the solid-electrolyte-electrode interface, *Nat. Commun.* 8 (2017) 1086.
- [18] T. Bernges, S.P. Culver, N. Minafra, R. Koerber, W.G. Zeier, Competing structural influences in the Li superionic conducting argyrodites  $\text{Li}_6\text{PS}_5-x\text{Se}x\text{Br}$  ( $0 \leq x \leq 1$ ) upon Se substitution, *Inorg. Chem.* 57 (2018) 13920–13928.

- [19] M.A. Kraft, S. Ohno, T. Zinkevich, R. Koerver, S.P. Culver, T. Fuchs, A. Senyshyn, S. Indris, B.J. Morgan, W.G. Zeier, Inducing high ionic conductivity in the lithium superionic argyrodites  $\text{Li}_6+\text{xP1-xGexS5I}$  for all-solid-state batteries, *J. Am. Chem. Soc.* 140 (2018) 16330–16339.
- [20] N. Minafra, S.P. Culver, T. Krauskopf, A. Senyshyn, W.G. Zeier, Effect of Si substitution on the structural and transport properties of superionic Li-argyrodites, *J. Mater. Chem. A* 6 (2018) 645–651.
- [21] R. Schlem, M. Ghidui, S.P. Culver, A.-L. Hansen, W.G. Zeier, Changing the static and dynamic lattice effects for the improvement of the ionic transport properties within the argyrodite  $\text{Li}_6\text{PS}_5\text{-x Se x I}$ , *ACS Appl. Energy Mater.* 3 (2020) 9–18.
- [22] S. Ohno, B. Helm, T. Fuchs, G. Dewald, M.A. Kraft, S.P. Culver, A. Senyshyn, W.G. Zeier, Further evidence for energy landscape flattening in the superionic argyrodites  $\text{Li}_6+\text{xP1-xMxS5I}$  (M= Si, Ge, Sn), *Chem. Mater.* 31 (2019) 4936–4944.
- [23] P. Adeli, J.D. Bazak, K.H. Park, I. Kochetkov, A. Huq, G.R. Goward, L.F. Nazar, Boosting solid-state diffusivity and conductivity in lithium superionic argyrodites by halide substitution, *Angew. Chem. Int. Ed.* 58 (2019) 8681–8686.
- [24] C. Yu, Y. Li, M.J. Willans, Y. Zhao, K.R. Adair, F. Zhao, W. Li, S. Deng, J. Liang, M.N. Banis, Superionic conductivity in lithium argyrodite solid-state electrolyte by controlled Cl-doping, *Nano Energy* (2019) 104396.
- [25] A. Varzi, R. Raccichini, S. Passerini, B. Scrosati, Challenges and prospects of the role of solid electrolytes in the revitalization of lithium metal batteries, *J. Mater. Chem. A* 4 (2016) 17251–17259.
- [26] Y. Huang, B. Chen, J. Duan, F. Yang, T. Wang, Z. Wang, W. Yang, C. Hu, W. Luo, Y. Huang, g-C<sub>3</sub>N<sub>4</sub>: an interface enabler for solid-state lithium metal batteries, *Angew. Chem. Int. Ed.* 59 (2020) 3699–3704.
- [27] J. Wen, Y. Huang, J. Duan, Y. Wu, W. Luo, L. Zhou, C. Hu, L. Huang, X. Zheng, W. Yang, Highly adhesive Li-bn nanosheet composite anode with excellent interfacial compatibility for solid-state Li metal batteries, *ACS Nano* 13 (2019) 14549–14556.
- [28] T. Cheng, B.V. Merinov, S. Morozov, W.A. Goddard III, Quantum mechanics reactive dynamics study of solid Li-electrode/Li<sub>6</sub>PS<sub>5</sub>Cl-electrolyte interface, *ACS Energy Lett.* 2 (2017) 1454–1459.
- [29] J. Auvergniot, A. Cassel, D. Foix, V. Viallet, V. Seznec, R. Dedryvère, Redox activity of argyrodite Li<sub>6</sub>PS<sub>5</sub>Cl electrolyte in all-solid-state Li-ion battery: an XPS study, *Solid State Ionics* 300 (2017) 78–85.
- [30] S. Wenzel, S.J. Sedlmaier, C. Dietrich, W.G. Zeier, J. Janek, Interfacial reactivity and interphase growth of argyrodite solid electrolytes at lithium metal electrodes, *Solid State Ionics* 318 (2018) 102–112.
- [31] J. Auvergniot, A. Cassel, J.-B. Ledeuil, V. Viallet, V. Seznec, R. Dedryvère, Interface stability of argyrodite Li<sub>6</sub>PS<sub>5</sub>Cl toward LiCoO<sub>2</sub>, LiNi<sub>1/3</sub>Co<sub>1/3</sub>Mn<sub>1/3</sub>O<sub>2</sub>, and LiMn<sub>2</sub>O<sub>4</sub> in bulk all-solid-state batteries, *Chem. Mater.* 29 (2017) 3883–3890.
- [32] J. Zhang, C. Zheng, J. Lou, Y. Xia, C. Liang, H. Huang, Y. Gan, X. Tao, W. Zhang, Poly (ethylene oxide) reinforced Li<sub>6</sub>PS<sub>5</sub>Cl composite solid electrolyte for all-solid-state lithium battery: enhanced electrochemical performance, mechanical property and interfacial stability, *J. Power Sources* 412 (2019) 78–85.
- [33] B. Wang, Y. Zhao, M.N. Banis, Q. Sun, K.R. Adair, R. Li, T.-K. Sham, X. Sun, Atomic layer deposition of lithium niobium oxides as potential solid-state electrolytes for lithium-ion batteries, *ACS Appl. Mater. Interfaces* 10 (2018) 1654–1661.
- [34] N.J. de Klerk, I. Rosloń, M. Wagemaker, Diffusion mechanism of Li argyrodite solid electrolytes for Li-ion batteries and prediction of optimized halogen doping: the effect of Li vacancies, halogens, and halogen disorder, *Chem. Mater.* 28 (2016) 7955–7963.
- [35] C. Yu, J. Hageman, S. Ganapathy, L. van Eijck, L. Zhang, K.R. Adair, X. Sun, M. Wagemaker, Tailoring Li<sub>6</sub>PS<sub>5</sub>Br ionic conductivity and understanding of its role in cathode mixtures for high performance all-solid-state Li-S batteries, *J. Mater. Chem. A* 7 (2019) 10412–10421.
- [36] S. Yubuchi, M. Uematsu, M. Deguchi, A. Hayashi, M. Tatsumisago, Lithium-ion-conducting argyrodite-type Li<sub>6</sub>PS<sub>5</sub>X (X= Cl, Br, I) solid electrolytes prepared by a liquid-phase technique using ethanol as a solvent, *ACS Appl. Energy Mater.* 1 (2018) 3622–3629.
- [37] S. Yubuchi, S. Teragawa, K. Aso, K. Tadanaga, A. Hayashi, M. Tatsumisago, Preparation of high lithium-ion conducting Li<sub>6</sub>PS<sub>5</sub>Cl solid electrolyte from ethanol solution for all-solid-state lithium batteries, *J. Power Sources* 293 (2015) 941–945.
- [38] W. Li, M. Li, Y. Hu, J. Lu, A. Lushington, R. Li, T. Wu, T.K. Sham, X. Sun, Synchrotron-based X-ray absorption fine structures, X-ray diffraction, and X-ray microscopy techniques applied in the study of lithium secondary batteries, *Small Methods* 2 (2018) 1700341.
- [39] F. Lin, Y. Liu, X. Yu, L. Cheng, A. Singer, O.G. Shpyrko, H.L. Xin, N. Tamura, C. Tian, T.-C. Weng, Synchrotron X-ray analytical techniques for studying materials electrochemistry in rechargeable batteries, *Chem. Rev.* 117 (2017) 13123–13186.
- [40] R. Koerver, F. Walther, I. Aygün, J. Sann, C. Dietrich, W.G. Zeier, J. Janek, Redox-active cathode interphases in solid-state batteries, *J. Mater. Chem. A* 5 (2017) 22750–22760.
- [41] J.M. Doux, H. Nguyen, D.H. Tan, A. Banerjee, X. Wang, E.A. Wu, C. Jo, H. Yang, Y.S. Meng, Stack pressure considerations for room-temperature all-solid-state lithium metal batteries, *Adv. Energy Mater.* 10 (2020) 1903253.
- [42] C. Yu, G. Li, X. Guan, J. Zheng, D. Luo, L. Li, The impact of upper cut-off voltages on the electrochemical behaviors of composite electrode 0.3 Li<sub>2</sub>MnO<sub>3</sub>-0.7 LiMn<sub>1/3</sub>Ni<sub>1/3</sub>Co<sub>1/3</sub>O<sub>2</sub>, *Phys. Chem. Chem. Phys.* 14 (2012) 12368–12377.